IEEE Access
Multidisciplinary | Rapid Review | Open Access Journal

SPECIAL SECTION ON EMERGING TRENDS, ISSUES AND CHALLENGES FOR ARRAY SIGNAL PROCESSING AND ITS APPLICATIONS IN SMART CITY

Received September 4, 2019, accepted October 14, 2019, date of publication October 21, 2019, date of current version November 1, 2019.

Digital Object Identifier 10.1109/ACCESS.2019.2948507

Cognitive Anti-Deception-Jamming for Airborne Array Radar via Phase-Only Pattern Notching With Nested ADMM

CAI WEN[1], (Member, IEEE), YAN HUANG[2], (Member, IEEE), JIANXIN WU[3], JINYE PENG[1], YAN ZHOU[1], AND JIE LIU[4]

[1]School of Information Science and Technology, Northwest University, Xi'an 710127, China
[2]State Key Laboratory of Millimeter Waves, School of Information Science and Engineering, Southeast University, Nanjing 210096, China
[3]School of Electronics and Communication Engineering, Sun Yat-sen University, Guangzhou 510275, China
[4]CAST Xi'an Institute of Space Radio Technology, Xi'an 710100, China

Corresponding authors: Cai Wen (wencai@nwu.edu.cn) and Jinye Peng (pjy@nwu.edu.cn)

This work was supported by the National Natural Science Foundation of China under Grant 61801383, Grant 61901371 and Grant 61901112. This work was also supported in part by the China Postdoctoral Science Foundation under Grant 2018M641009, in part by the Natural Science Basic Research Program of Shaanxi under Grant 2019JQ-460, in part by the Scientific Research Plan of Education Department of Shaanxi Provincial Government under Grant 18JK0768, in part by the Natural Science Foundation of Jiangsu Province under Grant BK20190330 and in part by the Aeronautical Science Foundation of China under Grant 20182098002.

ABSTRACT Deceptive jamming may not only induce a large amount of false alarms and deteriorate the target detection performance, but also lead to degraded space-time adaptive processing (STAP) performance in an airborne radar. To tackle these issues, this paper proposes a cognitive transmitting scheme to counter the deceptive jamming for airborne array radar. The proposed approach is composed of two steps. The first step is the deceptive jamming perception. A specially designed high pulse repetition frequency (PRF) waveform is transmitted, and then the deceptive jamming is identified according to the angle clustering feature of the false targets. In the second step, the phase-only transmit pattern with notches at the jammers' directions is designed. The encountered pattern synthesis problem is nonconvex due to the fixed excitations constraint. To solve this problem, a nested alternating direction method of multipliers (N-ADMM) is proposed. With the developed approach, the radiated power at the jammers' directions is attenuated significantly. Therefore, the probing signal possesses the characteristic of low probability of intercept (LPI). Numerical examples are given to demonstrate the effectiveness of the proposed approach.

INDEX TERMS Airborne radar, deceptive jamming, pattern synthesis, electronic counter-countermeasures (ECCM), space-time adaptive processing (STAP), ADMM.

I. INTRODUCTION

Airborne radar is an effective sensor for providing long-range and wide-area ground moving targets reconnaissance or surveillance [1]–[3]. The airborne radar usually operates at a high altitude, which means it is easy to suffer from electronic attacks. The typical electronic attack includes suppressive jamming and deceptive jamming. The suppressive jamming will raise the noise level of radar system, and thus degrade the performance of target detection [4]. Different from the suppressive jamming, deceptive jamming can not only raise the detection threshold, but also mislead the radar system to track false targets [5]. Even worse, the radar data processor is easy to be saturated in the presence of dense false targets [6]. Generally, compared with the suppressive jamming, the deceptive jamming is more difficult to be eliminated or identified in a radar system. To counter deceptive jamming, various electronic counter-countermeasures (ECCM) have been proposed [7]–[17]. They can be categorized into two types, i.e., receive processing-based approaches and transmit modulation-based approaches.

The receive processing-based approaches try to filter or identify deceptive jamming based solely on the received signal [7]–[10]. Space-time adaptive processing (STAP) is a typical receive processing-based approach in an airborne radar [7]. It combines multiple spatial channels with multiple coherent pulses to realize clutter and jamming rejection. Since the locations of false targets are usually unpredictable

The associate editor coordinating the review of this manuscript and approving it for publication was Wei Liu.

in range domain, it is hard to obtain sufficient range samples used for deceptive jamming covariance matrix estimation. Therefore, STAP has limited performance in rejecting deceptive jamming. The polarization filtering-based approach has the ability to suppress deceptive jamming to some extent [8], but this approach needs extra polarization channels which will bring increased hardware cost. In addition, the motion feature and the phase noise of digital radio frequency memory (DFRM) could be used to identify deceptive jamming [9], [10]. However, these approaches can only distinguish the deceptive jamming from the true targets, and the negative impact of deceptive jamming on target detection is still existing.

Different from above receive processing-based approaches, the transmit modulation-based approaches try to modulate the probing signal or transmit pattern to reducing the probability of radar being jammed [11]–[17]. The frequency agile and waveform diversity-based approaches are effective transmit modulation-based anti-jamming schemes [11]–[13]. However, these schemes will complicate the radar signal. Moreover, their influence on suppression of space-time coupled clutter has not been considered. The transmit pattern notching with prior knowledge of jammers' directions is another typical transmit modulation-based approach [14]–[17]. The synthesized beampattern has low gains at the jammers' directions. Therefore, the probability of radar signal being intercepted could be reduced significantly. The greatest advantage of transmit pattern notching is that it will not complicate the probing waveforms and not change the space-time coupling characteristic of the ground clutter. Therefore, conventional STAP algorithms can achieve a satisfactory performance in this case. However, the problem of deceptive jamming identification and direction finding in a practical airborne radar system is rarely discussed in the existing literature.

The development trend of modern radar signal processing has gradually changed from data-based adaptive receiving processing to cognitive transmitting and cognitive receiving processing, that is, radar can adjust transmitting and receiving systems adaptively according to the electromagnetic environment. This kind of fully adaptive radar is referred to as cognitive radar [18]–[20]. The perception-action cycle of a cognitive radar is mainly composed of three steps, i.e., sensing the environment, deciding upon an appropriate action, and then adapting accordingly [20]. In this work, the problem of anti-deception jamming for airborne array radar is solved in a cognitive perspective. Specifically, in the perception stage, the perception waveform is rationally designed to sense the jamming environment. Considering that the clutter signal will deteriorate the performance of parameter estimation, a high pulse repetition frequency (PRF) waveform with a relatively large clutter-free region is devised to sense the deceptive jamming. Then, the number of jammers and corresponding directions is estimated according to the clustering feature of the false targets.

In the action stage, the transmit pattern is synthesized with notches at the jammers' directions. In order to simplify the hardware cost, we assume that only the phase of each antenna element is adjustable. The resulting problem is equivalent to a quadratically constrained linear programming (QCLP) problem with fixed amplitudes constraint, and thus, it is nonconvex. Unlike the existing approaches for phase-only pattern design using semi-definite relaxation (SDR) technique [16], [17], a nested alternating direction method of multipliers (N-ADMM) is proposed to tackle the nonconvex QCLP problem. More specifically, we first apply variable splitting to introduce auxiliary two-element real vectors for each angular response constraint [21]. In doing so, the original problem can be solved via tackling two subproblems iteratively. Note that one of the subproblems is still nonconvex due to the fixed amplitudes constraint. The ADMM is applied again to tackle this subproblem at each iteration. The original problem can be efficiently solved by the proposed N-ADMM without using the CVX toolbox [22]. With the proposed active anti-jamming scheme, the radiated power at the jammers' directions is attenuated significantly. Therefore, the probability of radar being jammed could be decreased significantly. Furthermore, the signal processing burden at the receiving end could be reduced effectively.

The main contributions of the proposed work are briefly summarized as follows.

i) We propose to counter the deceptive jamming for the airborne radar in a cognitive perspective. A full perception-action cycle is given.

ii) The criterion for sensing waveform parameter design is presented with enhanced environment perception capability.

iii) An algorithm for deceptive jamming identification and localization is devised based on the angle-clustering feature of false targets.

iv) A novel method, termed Nested ADMM (N-ADMM), is proposed to tackle the problem of phase-only pattern notching. The corresponding scheme for computational load reduction is also provided. Compared with the SDR-based approaches, the proposed N-ADMM requires less computation cost meanwhile owns better performance.

The remainder of this paper is organized as follows. Section II develops the signal model of airborne array radar. Section III elaborates the proposed cognitive anti-deception jamming scheme. Section IV gives some discussions on the proposed approach. Simulation results are presented to verify the effectiveness of the proposed algorithm in section V, while the conclusions are drawn in section VI.

Notations: Vectors and matrices are denoted by boldface lowercase and uppercase letters, respectively. The $\mathrm{E}\{\,\}$, $\mathrm{diag}\{\,\}$, $\|\,\|$, $^{\mathrm{T}}$ and $^{\mathrm{H}}$ stand for the expectation, diagonalization, Frobenius norm, transpose and Hermitian transpose, respectively. The $\otimes$ and $\odot$ represent the Kronecker product and Hadamard product, respectively. The $\mathbf{I}_n$ denotes the $n \times n$ identity matrix, while $\Re\{\,\}$ and $\Im\{\,\}$ mean the real and imaginary parts, respectively.

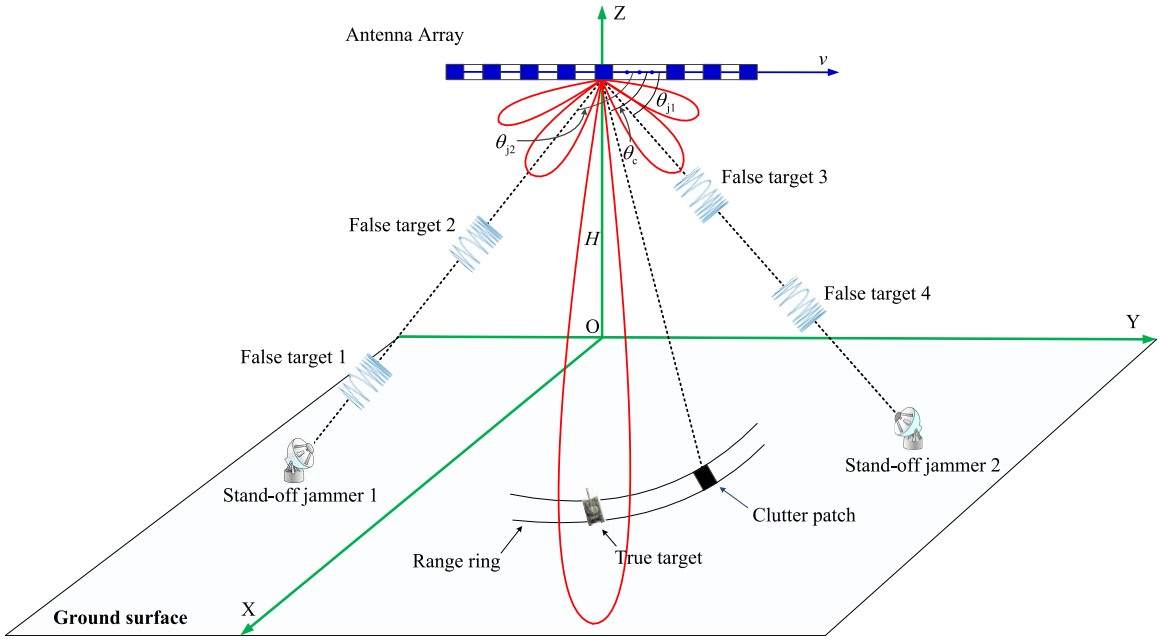

FIGURE 1. Operation geometry of airborne radar.

II. SIGNAL MODEL OF AIRBORNE ARRAY RADAR

Let us consider an airborne pulse-Doppler (PD) radar system that utilizes a N-element antenna array with interelement spacing d, and a K-pulse narrowband coherent waveform with pulse-repetition-interval (PRI) T_{p}. Fig. 1 depicts the operational geometry of an airborne radar. Only the sidelobe jamming is considered in this work. The antenna array is a sidelooking array whose axis is aligned with the flight direction. The height of the radar is H and the speed of the platform is v.

After matched filtering, the received space-time snapshot of the target can be expressed as [7]

$$\mathbf{x}_{\mathrm{t}} = \alpha_{\mathrm{t}}\mathbf{a}\left(\vartheta_{\mathrm{t}}\right) \otimes \mathbf{b}\left(\varpi_{\mathrm{t}}\right), \tag{1}$$

where α_{t} is the complex amplitude of the target, $\mathbf{a}\left(\vartheta_{\mathrm{t}}\right)$ and $\mathbf{b}\left(\varpi_{\mathrm{t}}\right)$ denote the spatial steering vector and temporal steering vector respectively, which are given by

$$\mathbf{a}\left(\vartheta_{\mathrm{t}}\right) = \left[1, \exp\left\{j2\pi\vartheta_{\mathrm{t}}\right\}, \cdots, \exp\left\{j\left(N-1\right)2\pi\vartheta_{\mathrm{t}}\right\}\right]^{\mathrm{T}}, \tag{2}$$

$$\mathbf{b}\left(\varpi_{\mathrm{t}}\right) = \left[1, \exp\left\{j2\pi\varpi_{\mathrm{t}}\right\}, \cdots, \exp\left\{j\left(K-1\right)2\pi\varpi_{\mathrm{t}}\right\}\right]^{\mathrm{T}}, \tag{3}$$

where $\vartheta_{\mathrm{t}} = d\cos\theta_{\mathrm{t}}/\lambda$ is the normalized spatial frequency, $\varpi_{\mathrm{t}} = 2v_{\mathrm{t}}T_{\mathrm{p}}/\lambda$ denotes the normalized Doppler frequency, λ represents the wavelength, θ_{t} and v_{t} stand for the direction of arrival (DOA) and radial velocity of the target.

According to the general clutter model introduced in [7], the clutter return from each ambiguous range can be modeled as the superposition of many independent clutter sources. Therefore, the space-time snapshot of the clutter can be expressed as

$$\mathbf{x}_{\mathrm{c}} = \sum_{p=1}^{N_{\mathrm{a}}}\sum_{q=1}^{N_{\mathrm{c}}}\alpha_{p\,q}\mathbf{a}\left(\vartheta_{pq}\right) \otimes \mathbf{b}\left(\varpi_{pq}\right), \tag{4}$$

where N_{a} is the number of range ambiguities, N_{c} is the number of clutter patches, $\alpha_{p\,q}$ is the complex amplitude of the clutter patch, $\vartheta_{pq} = d\cos\theta_{pq}/\lambda$ and $\varpi_{pq} = 2T_{\mathrm{p}}v\cos\theta_{pq}/\lambda$ are normalized spatial frequency and normalized Doppler frequency of the clutter patch respectively, and θ_{pq} is the DOA of the clutter patch.

The DFRM repeat jammer has the ability to intercept and store the radar signal, and modulate the intercepted signal with arbitrary delay and Doppler [5]. Therefore, the coherent repeater jammer is able to generate plenty of false targets, namely, deceptive jamming. Since the waveforms of false targets are very similar to that of true target, the deceptive jamming is very easy to obtain a high processing gain of matched filtering in the radar's receiver. Similar to the target snapshot, the space-time snapshot of deceptive jamming can be expressed as

$$\mathbf{x}_{\mathrm{j}} = \sum_{m=1}^{M}\sum_{i=1}^{P_m}\alpha_{\mathrm{j},mi}\mathbf{a}\left(\vartheta_{\mathrm{j},m}\right) \otimes \mathbf{b}\left(\varpi_{\mathrm{j},mi}\right), \tag{5}$$

where M is number of jammers, P_m denotes the number of false targets generated by the m-th jammer, $\vartheta_{\mathrm{j},m}$ stands for the normalized spatial frequency of the m-th jammer, $\alpha_{\mathrm{j},mi}$ and $\varpi_{\mathrm{j},mi}$ are the complex amplitude and normalized Doppler frequency of the false target, respectively. It is worth noting that the false targets generated by the same jammer share the same spatial frequency.

According to aforementioned definitions, if the range bin of interest contains a true target and deceptive jamming, then the received space-time snapshot can be expressed as

$$\mathbf{x} = \mathbf{x}_{\mathrm{t}} + \mathbf{x}_{\mathrm{c}} + \mathbf{x}_{\mathrm{j}} + \mathbf{x}_{\mathrm{n}}, \tag{6}$$

where $\mathbf{x}_n$ is the noise component. We assume that the noise snapshot $\mathbf{x}_n$ is a zero-mean complex Gaussian random vector with covariance matrix given by $\sigma_n^2\mathbf{I}_{NK}$, where σ_n^2 is the noise power.

The STAP technique is a critical data-based receiving processing technique in an airborne array radar [1]. It combines multiple spatial channels with coherent pulses to realize clutter and jamming rejection, provided that the statistical property of clutter and jamming could be estimated correctly. However, in the deceptive jamming scenario, the false targets are randomly and sparsely distributed in range-Doppler domain. In this case, the space-time dataset will become a non-homogeneous dataset. On one hand, to improve the performance of STAP in non-homogeneous environment, the STAP algorithms are usually carried out combined with non-homogeneous detector (NHD) [23]. That is to say, the false target contaminated samples will be removed from the dataset before STAP. Thus, the statistical property of deceptive jamming is hard to be correctly estimated in this case. On the other hand, if the STAP algorithms are performed without using NHD, the statistical property of deceptive jamming is still hard to be estimated correctly (especially the power of jamming), because the false targets are randomly and sparsely distributed in range domain. In summary, it is hard to obtain sufficient training data to estimate the statistical property of deceptive jamming. Therefore, STAP has limited performance in deceptive jamming suppression. The residual false targets will introduce a large amount of false alarms, which would bring heavy computational load to subsequent data processing. In the next section, a scheme of cognitive anti-deception jamming will be introduced to circumvent the above mentioned problem.

III. COGNITIVE-TRANSMIT-BASED ANTI-DECEPTION JAMMING

In this section, we introduce a cognitive transmit-based anti-deception jamming scheme. The block diagram of the proposed scheme is shown in Fig. 2. It is mainly composed of two parts, i.e., deceptive jamming perception and transmit pattern notching. The details of these two parts will be introduced in the following subsections.

A. DECEPTIVE JAMMING PERCEPTION FOR AIRBORNE ARRAY RADAR

In the perception stage, two fundamental missions should be accomplished: (1) sense and recognize deceptive jamming and (2) estimate the directions of jammers both in clutter-contaminated environment. To this end, a burst of sensing pulses with specially designed waveform is transmitted. Then, the targets (including true targets and false targets) are detected from the sensing data, and the DOAs of the detected targets are estimated. Further, the deceptive jamming can be identified according to the clustering feature of the estimated DOAs, meanwhile the number of jammers could be determined. The detailed steps for deceptive jamming perception are given as follows.

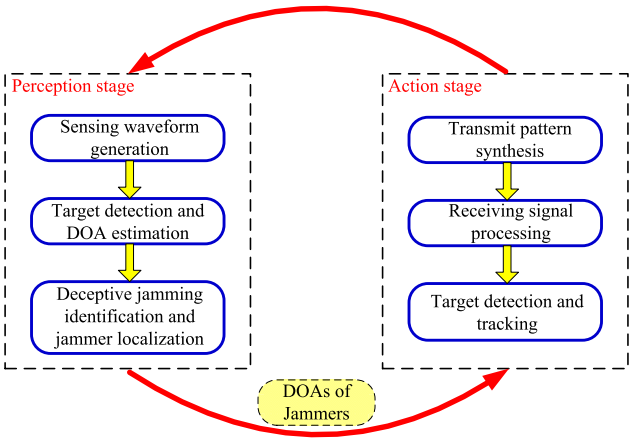

FIGURE 2. Block diagram of the proposed cognitive transmit-based anti-deception jamming scheme.

Step 1 (Sensing Waveform Parameter Design and Target Detection): Generally, the ground clutter of an airborne radar would spread in Doppler domain due to platform motion. As a consequence, a large proportion of Doppler region may be occupied by the ground clutter when the radar system operates at low- or mid-PRF. The probability of target detection and the accuracy of DOA estimation will degrade if the target is located in clutter region. In order to improve the performance of deceptive jamming perception, it is reasonable to employ high-PRF waveform. In high-PRF case, the clutter-free region is relatively large. Therefore, the false targets (i.e., deceptive jamming) will be located in clutter-free region with a high probability.

According to the observation geometry in Fig. 1, the Doppler bandwidth of the ground clutter is

$$B_d = 4v/\lambda. \tag{7}$$

Therefore, the PRF of the sensing waveform should be larger than B_d. However, the upper bound of PRF should not be infinite. Because that the higher the PRF is, the fewer the range bins are. If there exist a large amount of false targets, the number of range bins available for background level estimation would become very small in large PRF case. As a result, the target detection performance will suffer from significant degradation. In this work, as a rule of thumb, the PRF of the sensing waveform is set as $2B_d$ to $4B_d$ to reserve a relatively large clutter-free region and sufficient range bins. The other parameters of sensing waveform could be set to be the same as that of probing waveform.

After matched filtering, the received sensing data can be expressed as (6). In order to detect the false targets, the received data is firstly transformed into range-Doppler domain via PD processing. The PD processing is actually the non-adaptive space-time filtering. Therefore, for the target with normalized spatial frequency ϑ_0, the output of the $\bar{k}$-th Doppler bin corresponding to the l-th range bin can be expressed as

$$\tilde{y}_{\bar{k}l} = \left[\mathbf{a}\left(\vartheta_0\right) \otimes \left(\mathbf{q} \odot \mathbf{b}\left(\varpi_{\bar{k}}\right)\right)\right]^{\mathrm{H}} \mathbf{x}_l, \tag{8}$$

where $\bar{k} = 1, 2, \cdots, \bar{K}$ and $\bar{K}$ is the number of Doppler bins which could be selected as $\bar{K} = 2^{\lceil \log_2 K \rceil}$, $l = 1, 2, \cdots, L$ and L is the number of range bins, $\varpi_{\bar{k}} = (\bar{k} - 1)/\bar{K}$ denotes the normalized Doppler frequency of the $\bar{k}$-th Doppler bin, $\mathbf{q} \in \mathbb{R}^{K \times 1}$ is the temporal taper vector, e.g., Chebyshev or Taylor window.

Then, we can perform CFAR detection in range-Doppler domain. Considering that the performance of cell-averaging CFAR (CA-CFAR) detector degrades rapidly in nonideal conditions caused by multiple interfering targets (i.e. multiple false targets scenario considered in this paper), the ordered-statistic CFAR (OS-CFAR) is a reasonable alternative to the CA-CFAR [24]. The OS-CFAR trades a small loss in detection performance relative to the CA-CFAR in ideal conditions for much less performance degradation in nonideal conditions [25]. Define a set consisting of the coordinates of the detected targets in range-Doppler map, i.e.,

$$\Lambda = \left\{ (\bar{k}, l) \left| |\tilde{y}_{\bar{k}l}| \geq \xi \right. \right\}, \tag{9}$$

where $\xi = TZ$ is the detection threshold, Z is the averaging background level which is estimated by the l_0-th largest element of the rank-ordered magnitudes of L_0 reference cells, T is the threshold factor which can be determined by the probability of false alarm, l_0 and L_0 [24], i.e.,

$$p_{\mathrm{fa}} = l_0 \binom{L_0}{l_0} \frac{\Gamma(l_0)\Gamma(T + L_0 - l_0 + 1)}{\Gamma(T + L_0 + 1)}, \tag{10}$$

where $\Gamma(x) = \int_0^{+\infty} \mathrm{e}^{-t} t^{x-1} dt$ is the Gamma function of x.

Fig. 3 illustrates the possible situations of the detected targets. It is shown that the detected targets may be located in clutter region or in clutter-free region (with a high possibility).

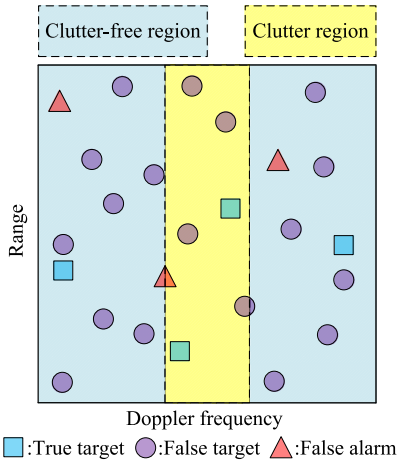

FIGURE 3. Possible locations of the detected targets in range-Doppler map.

Step 2 (DOA Estimation): As shown in Fig.3, the detected targets are separable in range-Doppler domain, thus the DOA of the detected target can be estimated in post-Doppler element space. There exist a lot of DOA estimation methods, such as subspace-based methods [26]–[28], compressive sensing-based methods [29], [30], maximum likelihood-based (ML) methods [31], [32] and so on. Among these methods, only the ML-based methods are capable of handling the interference (such as ground clutter). Therefore, in this paper, the ML method is utilized to estimate the DOA.

The spatial data vector of the $\bar{k}$-th Doppler bin can be obtained as

$$\tilde{\mathbf{x}}_{\bar{k}l} = \left[\mathbf{I}_N \otimes \left(\mathbf{q} \odot \mathbf{b}\left(\varpi_{\bar{k}} \right) \right) \right]^{\mathrm{H}} \mathbf{x}_l. \tag{11}$$

According to the ML estimation theory [31], the normalized target spatial frequency can be estimated by

$$\hat{\vartheta}_{\bar{k}l} = \arg \max_{\vartheta} \frac{\mathbf{a}^{\mathrm{H}}(\vartheta) \hat{\mathbf{R}}_{\bar{k}}^{-1} \tilde{\mathbf{x}}_{\bar{k}l} \tilde{\mathbf{x}}_{\bar{k}l}^{\mathrm{H}} \hat{\mathbf{R}}_{\bar{k}}^{-1} \mathbf{a}(\vartheta)}{\mathbf{a}^{\mathrm{H}}(\vartheta) \hat{\mathbf{R}}_{\bar{k}}^{-1} \mathbf{a}(\vartheta)}, \quad (\bar{k}, l) \in \Lambda, \tag{12}$$

where $\hat{\mathbf{R}}_{\bar{k}}$ is the interference-plus-noise covariance matrix of the $\bar{k}$-th Doppler bin. When the target is located in clutter-free region, the covariance matrix $\hat{\mathbf{R}}_{\bar{k}}$ could be replaced by the noise covariance matrix, i.e.,

$$\hat{\mathbf{R}}_{\bar{k}} = \sigma_{\mathrm{n}}^2 \mathbf{I}_N. \tag{13}$$

If the detected target is located in clutter region, the covariance matrix $\hat{\mathbf{R}}_{\bar{k}}$ should be estimated by the clutter samples, that is

$$\hat{\mathbf{R}}_{\bar{k}} = \frac{1}{\tilde{L}_0} \sum_{l=1, l \notin \Lambda}^{L} \tilde{\mathbf{x}}_{\bar{k}l} \tilde{\mathbf{x}}_{\bar{k}l}^{\mathrm{H}}, \tag{14}$$

where $\tilde{L}_0 = \sum_{l=1, l \notin \Lambda}^{L} l$ is the number of available clutter samples. It should be noted that the interfering targets included in $\hat{\mathbf{R}}_{\bar{k}}$ will lead to significant DOA estimation performance degradation. Therefore, the range samples which contain the interfering targets are discarded in the process of estimating $\hat{\mathbf{R}}_{\bar{k}}$.

Step 3 (Deceptive Jamming Identification and Jammer Localizatio): It can be seen from (5) that the false targets generated by the same jammer share the same DOA. It means that the estimated false target DOAs will concentrate in the angle regions where the jammers are. Hence, the deceptive jamming could be recognized according to the number of targets in a given angle region. Specifically, given the angle region $[\hat{\vartheta}_{\bar{k}l} - \Delta\vartheta, \hat{\vartheta}_{\bar{k}l} + \Delta\vartheta]$ (where $(\bar{k}, l) \in \Lambda$) and a threshold $N_{\min}$, if the target number $N_{\bar{k}l}$ in the angle region $[\hat{\vartheta}_{\bar{k}l} - \Delta\vartheta, \hat{\vartheta}_{\bar{k}l} + \Delta\vartheta]$ exceeds $N_{\min}$, we conclude that there may exist a jammer in this angle region. The detailed algorithm for jammer localization is summarized in Table 1. Some remarks on the proposed algorithm are given as follows.

Remark 1: At the input stage, the true targets are removed, i.e., only the targets outside of mainlobe are processed.

Remark 2: The parameter $\Delta\vartheta$ is selected as $\vartheta_{3\mathrm{dB}}/10$ to account for the deviation of estimated DOA, where $\vartheta_{3\mathrm{dB}}$ is the beamwidth.

Remark 3: The parameter $N_{\min}$ is selected as 3. A possible scenario is that there may be more than 3 sidelobe true targets

TABLE 1. Proposed angle clustering feature-based jammer localization algorithm.

Input: $\hat{\vartheta}_{\bar{k}\,l}, (\bar{k}, l) \in \Lambda$, where $\hat{\vartheta}_{\bar{k}\,l}$ is selected from outside of mainbeam.
Procedure:
1) Counting: count the number of targets $N_{\bar{k}\,l}$ in angle region $[\hat{\vartheta}_{\bar{k}\,l} - \Delta\vartheta, \hat{\vartheta}_{\bar{k}\,l} + \Delta\vartheta]$;
2) Selecting: select the target DOA which satisfies $N_{\bar{k}\,l} > N_{\min}$, i.e., $\hat{\vartheta}_{\bar{k}\,l}, (\bar{k}, l) \in \bar{\Lambda} = \left\{(\bar{k}, l) \middle| (\bar{k}, l) \in \Lambda, N_{\bar{k}\,l} > N_{\min}\right\}$;
3) Clustering: if the space between two adjacent DOAs ($\hat{\vartheta}_{\bar{k}\,l}, (\bar{k}, l) \in \bar{\Lambda}$) is less than $\Delta\vartheta$, they are considered to be generated by the same jammer;
4) Calculating: calculate the average DOA $\bar{\vartheta}_{\mathrm{j},m}$ of every class (corresponding to the m-th jammer).
Output: directions of M jammers, i.e., $\bar{\vartheta}_{\mathrm{j},m}$, $m = 1, \cdots, M$.

appearing at the same angle region. In this case, the synthesized beampattern will introduce an additional notch at this angle region. (In practice, the possibility of multiple sidelobe true targets appearing at the same angle region is very small).

B. TRANSMIT PATTERN NOTCHING USING N-ADMM

In the action stage, the transmit pattern is synthesized to produce notches at the jammers' directions. Herein, in order to simplify the hardware structure, the notches are generated via phase-only weight control. That is to say, the shaped beampattern could be generated by only adjusting the phase of each antenna element.

The problem of phase-only beampattern synthesis can be formulated as maximizing the mainbeam gain under the weight amplitude constraint and angular response constraint, that is

$$\begin{aligned} &\max_{\mathbf{w}} \left|\mathbf{w}^{\mathrm{H}}\mathbf{a}\left(\vartheta_0\right)\right| \\ &\text{s.t. } |w_n| = c_n, \quad n = 1, \cdots, N \\ &\quad \left|\mathbf{w}^{\mathrm{H}}\mathbf{a}\left(\bar{\vartheta}_{\mathrm{j},m}\right)\right|^2 \le U_m, \quad m = 1, \cdots, M. \end{aligned} \tag{15}$$

where $\mathbf{w} = [w_1, w_2, ..., w_N]^{\mathrm{T}} \in \mathbb{C}^{N\times 1}$ is the so-called weight vector, $\{c_n\}_{n=1}^N$ are the amplitudes of the weighting factors $\{w_n\}_{n=1}^N$, U_m stands for the upper bound of the corresponding radiated power. By introducing an auxiliary variable η, (15) could be equivalently formulated as a minimization problem:

$$\begin{aligned} &\min_{\mathbf{w},\eta} \eta \\ &\text{s.t. } \left|\mathbf{w}^{\mathrm{H}}\mathbf{a}\left(\vartheta_0\right)\right| \ge -\eta, \eta < 0 \\ &\quad \left|\mathbf{w}^{\mathrm{H}}\mathbf{a}\left(\bar{\vartheta}_{\mathrm{j},m}\right)\right|^2 \le U_m, \quad m = 1, \cdots, M \\ &\quad |w_n| = c_n, \quad n = 1, \cdots, N. \end{aligned} \tag{16}$$

Actually, (16) is a QCLP problem, but it is nonconvex due to the first and the third constraints. In order to solve this problem, a N-ADMM is proposed. This algorithm is based on the idea that multiple inequality constraints could be associated with different optimization variables so that they can be tackled separately [21]. More specifically, we first introduce real-valued two-element auxiliary vectors

$$\mathbf{y}_0 = \mathbf{A}\left(\vartheta_0\right)\tilde{\mathbf{w}} \in \mathbb{R}^{2\times 1} \tag{17}$$

$$\mathbf{y}_m = \mathbf{A}\left(\bar{\vartheta}_{\mathrm{j},m}\right)\tilde{\mathbf{w}} \in \mathbb{R}^{2\times 1}, \quad m = 1, \cdots, M, \tag{18}$$

where

$$\tilde{\mathbf{w}} = \begin{bmatrix} \Re\{\mathbf{w}\} \\ \Im\{\mathbf{w}\} \end{bmatrix} \tag{19}$$

$$\mathbf{A}\left(\vartheta_0\right) = \begin{bmatrix} \Re\left\{\mathbf{a}^{\mathrm{T}}\left(\vartheta_0\right)\right\} & -\Im\left\{\mathbf{a}^{\mathrm{T}}\left(\vartheta_0\right)\right\} \\ \Im\left\{\mathbf{a}^{\mathrm{T}}\left(\vartheta_0\right)\right\} & \Re\left\{\mathbf{a}^{\mathrm{T}}\left(\vartheta_0\right)\right\} \end{bmatrix} \tag{20}$$

and $\mathbf{A}\left(\bar{\vartheta}_{\mathrm{j},m}\right)$ is defined in the same manner. With these definitions, (16) becomes

$$\begin{aligned} &\min_{\mathbf{w},\eta} \eta \\ &\text{s.t. } \mathbf{y}_0 = \mathbf{A}\left(\vartheta_0\right)\tilde{\mathbf{w}} \\ &\quad \mathbf{y}_m = \mathbf{A}\left(\bar{\vartheta}_{\mathrm{j},m}\right)\tilde{\mathbf{w}}, \quad m = 1, \cdots, M \\ &\quad |\mathbf{y}_0|^2 \ge \eta^2, \quad \eta < 0 \\ &\quad |\mathbf{y}_m|^2 \le U_m, \quad m = 1, \cdots, M \\ &\quad \tilde{w}_n^2 + \tilde{w}_{n+N}^2 = c_n^2, \quad n = 1, \cdots, N. \end{aligned} \tag{21}$$

Define the augmented Lagrangian as

$$\begin{aligned} &\ell_{0,\rho}\left(\tilde{\mathbf{w}}, \eta, \mathbf{y}_0, \mathbf{y}_m, \boldsymbol{\lambda}_0, \boldsymbol{\lambda}_m\right) \\ &= \eta + \left(\boldsymbol{\lambda}_0^{\mathrm{T}}\left(\mathbf{y}_0 - \mathbf{A}\left(\vartheta_0\right)\tilde{\mathbf{w}}\right) + \frac{\rho}{2}\left\|\mathbf{y}_0 - \mathbf{A}\left(\vartheta_0\right)\tilde{\mathbf{w}}\right\|^2\right) \\ &\quad + \sum_{m=1}^{M}\left(\boldsymbol{\lambda}_m^{\mathrm{T}}\left(\mathbf{y}_m - \mathbf{A}\left(\bar{\vartheta}_{\mathrm{j},m}\right)\tilde{\mathbf{w}}\right) + \frac{\rho}{2}\left\|\mathbf{y}_m - \mathbf{A}\left(\bar{\vartheta}_{\mathrm{j},m}\right)\tilde{\mathbf{w}}\right\|^2\right), \end{aligned} \tag{22}$$

where $\boldsymbol{\lambda}_0 \in \mathbb{R}^{2\times 1}$ and $\boldsymbol{\lambda}_m \in \mathbb{R}^{2\times 1}$ are the Lagrange multiplier vectors, while $\rho > 0$ is a user-defined parameter representing the primal step size. Then all unknowns in (21) as well as $\boldsymbol{\lambda}_0$ and $\boldsymbol{\lambda}_m$ can be determined using the iterative manner of the ADMM from $\ell_{0,\rho}\left(\tilde{\mathbf{w}}, \eta, \mathbf{y}_0, \mathbf{y}_m, \boldsymbol{\lambda}_0, \boldsymbol{\lambda}_m\right)$:

Step 1: Update $\tilde{\mathbf{w}}$ with given $\left\{\eta^{(i)}, \mathbf{y}_0^{(i)}, \mathbf{y}_m^{(i)}, \boldsymbol{\lambda}_0^{(i)}, \boldsymbol{\lambda}_m^{(i)}\right\}$ (which are obtained from the i-th iteration) by solving

$$\begin{aligned} &\min_{\tilde{\mathbf{w}}}\left\{\eta^{(i)} + \left(\left(\boldsymbol{\lambda}_0^{(i)}\right)^{\mathrm{T}}\left(\mathbf{y}_0^{(i)} - \mathbf{A}\left(\vartheta_0\right)\tilde{\mathbf{w}}\right) + \frac{\rho}{2}\left\|\mathbf{y}_0^{(i)} - \mathbf{A}\left(\vartheta_0\right)\tilde{\mathbf{w}}\right\|^2\right)\right. \\ &\quad + \sum_{m=1}^{M}\left(\left(\boldsymbol{\lambda}_m^{(i)}\right)^{\mathrm{T}}\left(\mathbf{y}_m^{(i)} - \mathbf{A}\left(\bar{\vartheta}_{\mathrm{j},m}\right)\tilde{\mathbf{w}}\right)\right. \\ &\quad \left.\left. + \frac{\rho}{2}\left\|\mathbf{y}_m^{(i)} - \mathbf{A}\left(\bar{\vartheta}_{\mathrm{j},m}\right)\tilde{\mathbf{w}}\right\|^2\right)\right\} \\ &\text{s.t. } \tilde{w}_n^2 + \tilde{w}_{n+N}^2 = c_n^2, \quad n = 1, \cdots, N. \end{aligned} \tag{23}$$

Overlooking the terms independent of $\tilde{\mathbf{w}}$, (23) can be compactly rewritten as

$$\begin{aligned} &\min_{\tilde{\mathbf{w}}} \tilde{\mathbf{w}}^{\mathrm{T}}\mathbf{R}_1\tilde{\mathbf{w}} + \tilde{\mathbf{w}}^{\mathrm{T}}\mathbf{d}_1^{(i)} \\ &\text{s.t. } \tilde{w}_n^2 + \tilde{w}_{n+N}^2 = c_n^2, \quad n = 1, \cdots, N, \end{aligned} \tag{24}$$

where

$$\mathbf{R}_1 = \frac{\rho}{2}\mathbf{A}^{\mathrm{T}}\left(\vartheta_0\right)\mathbf{A}\left(\vartheta_0\right) + \frac{\rho}{2}\sum_{m=1}^{M}\mathbf{A}^{\mathrm{T}}\left(\bar{\vartheta}_{\mathrm{j},m}\right)\mathbf{A}\left(\bar{\vartheta}_{\mathrm{j},m}\right), \tag{25}$$

$$\mathbf{d}_1^{(i)} = -\mathbf{A}^{\mathrm{T}}\left(\vartheta_0\right)\left(\boldsymbol{\lambda}_0^{(i)} + \rho\mathbf{y}_0^{(i)}\right) - \sum_{m=1}^{M}\mathbf{A}^{\mathrm{T}}\left(\bar{\vartheta}_{\mathrm{j},m}\right)\left(\boldsymbol{\lambda}_m^{(i)} + \rho\mathbf{y}_m^{(i)}\right). \tag{26}$$

Note that (24) is still nonconvex due to the amplitude constraints. Actually, the amplitude constraints can be rewritten as multiple quadratic equality constraints. By doing so, (24) could also be solved by ADMM efficiently. The detailed procedure to update $\tilde{\mathbf{w}}$ is given in Appendix.

Step 2: Update $\{\eta, \mathbf{y}_0, \mathbf{y}_m\}$ with given $\left\{\tilde{\mathbf{w}}^{(i+1)}, \boldsymbol{\lambda}_0^{(i)}, \boldsymbol{\lambda}_m^{(i)}\right\}$ by solving

$$\begin{aligned}\min_{\eta,\mathbf{y}_0,\mathbf{y}_m}\Bigg\{&\eta+\left(\left(\boldsymbol{\lambda}_0^{(i)}\right)^{\mathrm{T}}\left(\mathbf{y}_0-\mathbf{A}\left(\vartheta_0\right)\tilde{\mathbf{w}}^{(i+1)}\right)\right.\\&\left.+\frac{\rho}{2}\left\|\mathbf{y}_0-\mathbf{A}\left(\vartheta_0\right)\tilde{\mathbf{w}}^{(i+1)}\right\|^2\right)\\&+\sum_{m=1}^{M}\left(\left(\boldsymbol{\lambda}_m^{(i)}\right)^{\mathrm{T}}\left(\mathbf{y}_m-\mathbf{A}\left(\bar{\vartheta}_{\mathrm{j},m}\right)\tilde{\mathbf{w}}^{(i+1)}\right)\right.\\&\left.+\frac{\rho}{2}\left\|\mathbf{y}_m-\mathbf{A}\left(\bar{\vartheta}_{\mathrm{j},m}\right)\tilde{\mathbf{w}}^{(i+1)}\right\|^2\right)\Bigg\}\\\text{s.t. }&|\mathbf{y}_0|^2\geq\eta^2,\quad\eta<0\\&|\mathbf{y}_m|^2\leq U_m,\quad m=1,\cdots,M.\end{aligned}\tag{27}$$

After removing the irrelevant terms, (27) can be rewritten as

$$\begin{aligned}\min_{\eta,\mathbf{y}_0,\mathbf{y}_m}\ &\left\{\eta+\frac{\rho}{2}\left\|\mathbf{y}_0-\tilde{\mathbf{y}}_0^{(i)}\right\|^2+\frac{\rho}{2}\sum_{m=1}^{M}\left\|\mathbf{y}_m-\tilde{\mathbf{y}}_m^{(i)}\right\|^2\right\}\\\text{s.t. }&|\mathbf{y}_0|^2\geq\eta^2,\quad\eta<0\\&|\mathbf{y}_m|^2\leq U_m,\quad m=1,\cdots,M,\end{aligned}\tag{28}$$

where $\tilde{\mathbf{y}}_0^{(i)}=\mathbf{A}\left(\vartheta_0\right)\tilde{\mathbf{w}}^{(i+1)}-\boldsymbol{\lambda}_0^{(i)}/\rho$ and $\tilde{\mathbf{y}}_m^{(i)}=\mathbf{A}\left(\bar{\vartheta}_{\mathrm{j},m}\right)\tilde{\mathbf{w}}^{(i+1)}-\boldsymbol{\lambda}_m^{(i)}/\rho$.

Note that $\mathbf{y}_m$ is independent of η and $\mathbf{y}_0$ in (28). Thus, (28) can be decomposed into two optimization subproblems, i.e.,

$$\begin{aligned}\min_{\mathbf{y}_m}\ &\frac{\rho}{2}\sum_{m=1}^{M}\left\|\mathbf{y}_m-\tilde{\mathbf{y}}_m^{(i)}\right\|^2\\\text{s.t. }&|\mathbf{y}_m|^2\leq U_m,\quad m=1,\cdots,M\end{aligned}\tag{29}$$

and

$$\begin{aligned}\min_{\eta,\mathbf{y}_0}\ &\eta+\frac{\rho}{2}\left\|\mathbf{y}_0-\tilde{\mathbf{y}}_0^{(i)}\right\|^2\\\text{s.t. }&|\mathbf{y}_0|^2\geq\eta^2,\quad\eta<0.\end{aligned}\tag{30}$$

Actually, (29) can be further separated into M subproblems, and the m-th subproblem is

$$\begin{aligned}\min_{\mathbf{y}_m}\ &\left\|\mathbf{y}_m-\tilde{\mathbf{y}}_m^{(i)}\right\|^2\\\text{s.t. }&|\mathbf{y}_m|^2\leq U_m.\end{aligned}\tag{31}$$

The solution of (31) is given by

$$\mathbf{y}_m^{(i+1)}=\begin{cases}\dfrac{\sqrt{U_m}}{\left\|\tilde{\mathbf{y}}_m^{(i)}\right\|}\tilde{\mathbf{y}}_m^{(i)}, & \left\|\tilde{\mathbf{y}}_m^{(i)}\right\|\geq\sqrt{U_m}\\ \tilde{\mathbf{y}}_m^{(i)}, & \left\|\tilde{\mathbf{y}}_m^{(i)}\right\|<\sqrt{U_m}.\end{cases}\tag{32}$$

However, for the subproblem (30), η is coupled with $\mathbf{y}_0$. Fortunately, with given $\eta<0$, it is readily shown that the minimum of $\left\|\mathbf{y}_0-\tilde{\mathbf{y}}_0^{(i)}\right\|^2$ can be calculated as

$$\min_{\mathbf{y}_0}\left\{\left\|\mathbf{y}_0-\tilde{\mathbf{y}}_0^{(i)}\right\|^2\right\}=\begin{cases}0, & \left\|\tilde{\mathbf{y}}_0^{(i)}\right\|\geq-\eta\\ \left(\eta+\left\|\tilde{\mathbf{y}}_0^{(i)}\right\|\right)^2, & \left\|\tilde{\mathbf{y}}_0^{(i)}\right\|<-\eta.\end{cases}\tag{33}$$

Therefore, by substituting (33) back into (30), (30) can be rewritten as a function of η, that is

$$\min_{\eta}\begin{cases}\eta, & -\left\|\tilde{\mathbf{y}}_0^{(i)}\right\|\leq\eta<0\\ \eta+\frac{\rho}{2}\left(\eta+\left\|\tilde{\mathbf{y}}_0^{(i)}\right\|\right)^2, & \eta<-\left\|\tilde{\mathbf{y}}_0^{(i)}\right\|.\end{cases}\tag{34}$$

Note that, when $-\left\|\tilde{\mathbf{y}}_0^{(i)}\right\|\leq\eta<0$, the minimum of (34) is

$$V_1=-\left\|\tilde{\mathbf{y}}_0^{(i)}\right\|.\tag{35}$$

The second row of (34) is a quadratic function of η which can be rewritten in a stand quadratic form, i.e.,

$$\begin{aligned}\min_{\eta}\ &\frac{\rho}{2}\left(\eta-\left(-\left\|\tilde{\mathbf{y}}_0^{(i)}\right\|-\frac{1}{\rho}\right)\right)^2-\frac{1}{2\rho}-\left\|\tilde{\mathbf{y}}_0^{(i)}\right\|\\\text{s.t. }&\eta<-\left\|\tilde{\mathbf{y}}_0^{(i)}\right\|.\end{aligned}\tag{36}$$

Since $-\left\|\tilde{\mathbf{y}}_0^{(i)}\right\|-1/\rho<-\left\|\tilde{\mathbf{y}}_0^{(i)}\right\|$ (because $\rho>0$), the minimum of (36) is

$$V_2=-\left\|\tilde{\mathbf{y}}_0^{(i)}\right\|-\frac{1}{2\rho}.\tag{37}$$

Obviously, $V_2<V_1$ (because $\rho>0$). Therefore, the optimal solution of (34) is dependent on (36). According to (36), we can determine the optimal η as

$$\eta^{(i+1)}=-\left\|\tilde{\mathbf{y}}_0^{(i)}\right\|-\frac{1}{\rho}.\tag{38}$$

Once $\eta^{(i+1)}$ is determined, the optimal $\mathbf{y}_0$ can be obtained by solving (30), that is

$$\mathbf{y}_0^{(i+1)}=-\frac{\eta^{(i+1)}}{\left\|\tilde{\mathbf{y}}_0^{(i)}\right\|}\tilde{\mathbf{y}}_0^{(i)}.\tag{39}$$

Step 3: Update $\boldsymbol{\lambda}_0$ and $\boldsymbol{\lambda}_m$ as

$$\boldsymbol{\lambda}_0^{(i+1)}=\boldsymbol{\lambda}_0^{(i)}+\rho\left(\mathbf{y}_0^{(i+1)}-\mathbf{A}\left(\vartheta_0\right)\tilde{\mathbf{w}}^{(i+1)}\right),\tag{40}$$

$$\boldsymbol{\lambda}_m^{(i+1)}=\boldsymbol{\lambda}_m^{(i)}+\rho\left(\mathbf{y}_m^{(i+1)}-\mathbf{A}\left(\bar{\vartheta}_{\mathrm{j},m}\right)\tilde{\mathbf{w}}^{(i+1)}\right).\tag{41}$$

Via iterating **Steps** 1 to 3, the proposed N-ADMM for transmit pattern notching is summarized in Table 2.

TABLE 2. Proposed nested ADMM for transmit pattern notching.

Initialization: $\{\mathbf{y}_0^{(0)}, \mathbf{y}_m^{(0)}, \boldsymbol{\lambda}_0^{(0)}, \boldsymbol{\lambda}_m^{(0)}\}$;
for i=1,…,I, where I is the predefined maximum iteration number.
Update $\tilde{\mathbf{w}}^{(i+1)}$ using the ADMM algorithm presented in Appendix;
Determine $\mathbf{y}_m^{(i+1)}$ using (32);
Determine $\eta^{(i+1)}$ and $\mathbf{y}_0^{(i+1)}$ using (38) and (39) respectively;
Update $\boldsymbol{\lambda}_0^{(i+1)}$ and $\boldsymbol{\lambda}_m^{(i+1)}$ using (40) and (41) respectively;
end for i=I or $\max_m \left\| \mathbf{y}_m^{(i+1)} - \mathbf{A}\left(\bar{\vartheta}_{j,m}\right)\tilde{\mathbf{w}}^{(i+1)} \right\| \le \Delta$, where $\Delta > 0$ is the tolerance parameter.
Output: weight vector $\mathbf{w}$ from $\tilde{\mathbf{w}}$.

IV. DISCUSSIONS

A. ON PRACTICAL IMPLEMENTATION

1) CPI LENGTH OF SENSE WAVEFORM

In the deceptive jamming perception stage, a burst of pulses is transmitted to sense the jamming environment. Actually, the CPI length of sense waveform could be shorter than that of normal probing waveform. This is because the false targets are much easier to be detected than the true target due to the large jamming power. In another words, the integration time of the sense waveform (i.e., the length of CPI) could be set as a small value (such as a half of the CPI of probing waveform). A short CPI will reduce the data throughput of the radar system and also reduce the consumption of time resource in perception stage.

2) NOTCH WIDTH

In the transmit pattern notching stage, we assumed the jamming is a point-like jamming. The synthesized pattern can only produce nulls at the estimated directions of the jammers. In practice, the DOA estimation algorithm will induce DOA deviation, meanwhile the platform motion also results in direction bias. Therefore, it is necessary to broaden the notches to some extent to handle these biases. In our numerical examples, all notches are widened to 3° via adding angle grids around the estimated DOAs of jammers.

B. ON COMPUTATIONAL COMPLEXITY OF N-ADMM

1) ANALYSIS ON COMPUTATIONAL COMPLEXITY OF N-ADMM

For each update of primal variable $\tilde{\mathbf{w}}$, we need to solve (24) via the inner ADMM algorithm. In the inner ADMM, the update of $\tilde{\mathbf{w}}$ includes calculating $\mathbf{d}_2^{(p)}$, $\mathbf{R}_2^{(p)}$ and the inverse of $\mathbf{R}_2^{(p)}$, which totally takes $O(10N^2 + 14N^3)$. Similarly, the update of $\mathbf{z}$ (using (A.19)) will also take $O(10N^2+14N^3)$. In addition, the update of $\boldsymbol{\beta}_2$ takes $O(2N^2)$. Therefore, solving (24) will take $O(\log(\varepsilon^{-1})(22N^2 + 28N^3))$ [33], where ε is a given accuracy of the inner ADMM algorithm. For each update of auxiliary variables $\{\eta, \mathbf{y}_0, \mathbf{y}_m\}$, it will take $O(2M)$. Therefore, the computational complexity of N-ADMM is $O(\log(\varepsilon^{-1})(22N^2 + 28N^3) + 2M)$ at each iteration.

2) COMPUTATIONAL COMPLEXITY REDUCTION SCHEME

Note that the computational complexity of N-ADMM at each iteration is mainly dependent on solving (24). More specifically, it depends on calculating $\mathbf{R}_2^{(p)}$ and $\mathbf{R}_3^{(p)}$ and the inverses of $\mathbf{R}_2^{(p)}$ and $\mathbf{R}_3^{(p)}$. By carefully examining $\mathbf{R}_2^{(p)}$ and $\mathbf{R}_3^{(p)}$, we find they are sparse matrices since $\mathbf{E}_n$ is a sparse diagonal matrix. Therefore, the computational complexity of N-ADMM could be reduced significantly using the sparse structure of $\mathbf{R}_2^{(p)}$ and $\mathbf{R}_3^{(p)}$.

Taking $\mathbf{R}_2^{(p)}$ as an example, according to (A.5), $\mathbf{B}\left(\mathbf{z}^{(p)}\right)$ can be rewritten as

$$\mathbf{B}\left(\mathbf{z}^{(p)}\right) = \left[\mathbf{D}_1^{(p)} \ \mathbf{D}_2^{(p)}\right], \tag{42}$$

where $\mathbf{D}_1^{(p)} = \mathrm{diag}\left\{z_1^{(p)}, \cdots, z_N^{(p)}\right\}$ and $\mathbf{D}_2^{(p)} = \mathrm{diag}\left\{z_{N+1}^{(p)}, \cdots, z_{2N}^{(p)}\right\}$. Substituting (42) into (A.10), $\mathbf{R}_2^{(p)}$ can be rewritten as

$$\begin{aligned}\mathbf{R}_2^{(p)} &= \rho_1\left(\mathbf{I}_{2N} + \left[\mathbf{D}_1^{(p)} \quad \mathbf{D}_2^{(p)}\right]^{\mathrm{T}}\left[\mathbf{D}_1^{(p)} \quad \mathbf{D}_2^{(p)}\right]\right)\\ &= \rho_1\left(\mathbf{I}_{2N} + \begin{bmatrix}\mathbf{D}_1^{(p)}\mathbf{D}_1^{(p)} & \mathbf{D}_1^{(p)}\mathbf{D}_2^{(p)}\\ \mathbf{D}_2^{(p)}\mathbf{D}_1^{(p)} & \mathbf{D}_2^{(p)}\mathbf{D}_2^{(p)}\end{bmatrix}\right)\\ &= \rho_1\begin{bmatrix}\tilde{\mathbf{D}}_1^{(p)} & \tilde{\mathbf{D}}_3^{(p)}\\ \tilde{\mathbf{D}}_3^{(p)} & \tilde{\mathbf{D}}_2^{(p)}\end{bmatrix},\end{aligned} \tag{43}$$

where $\tilde{\mathbf{D}}_1^{(p)} = \mathbf{I}_N + \mathrm{diag}\left\{(z_1^{(p)})^2, \cdots, (z_N^{(p)})^2\right\}$, $\tilde{\mathbf{D}}_2^{(p)} = \mathbf{I}_N + \mathrm{diag}\left\{(z_{N+1}^{(p)})^2, \cdots, (z_{2N}^{(p)})^2\right\}$ and $\tilde{\mathbf{D}}_3^{(p)} = \mathrm{diag}\left\{z_1^{(p)}z_{N+1}^{(p)}, \cdots, z_N^{(p)}z_{2N}^{(p)}\right\}$ are diagonal matrices.

It can be seen from (43) that $\mathbf{R}_2^{(p)}$ is actually a block matrix with 4 blocks being diagonal matrices. Evidently, the computational complexity of constructing $\mathbf{R}_2^{(p)}$ is reduced to $O(3N)$.

According to the matrix inversion lemma [34], the inverse of $\mathbf{R}_2^{(p)}$ can be easily computed with a closed-form solution, which is given by (44), as shown at the bottom of this page. Note that $(\mathbf{R}_2^{(p)})^{-1}$ is still a block matrix with 4 blocks being diagonal matrices. Therefore, the computational complexity of calculating $(\mathbf{R}_2^{(p)})^{-1}$ is only $O(11N)$. Similarly, the computational complexity of calculating $\mathbf{R}_3^{(p)}$ and $(\mathbf{R}_3^{(p)})^{-1}$ are $O(3N)$ and $O(11N)$, respectively.

In addition, using the sparse structure of the matrix, updating $\mathbf{d}_2^{(p)}$ and $\mathbf{d}_3^{(p)}$ only needs $O(8N^2 + 4N)$, while calculating $\tilde{\mathbf{w}}^{(p+1)}$ and $\mathbf{z}^{(p+1)}$ only takes $O(8N)$. In summary, if we utilize the sparse structure of the matrix, then solving (24) will only take $O(8N^2+40N)$. Therefore, the computational complexity

$$(\mathbf{R}_2^{(p)})^{-1} = \frac{1}{\rho_1}\begin{bmatrix}(\tilde{\mathbf{D}}_1^{(p)} - \tilde{\mathbf{D}}_3^{(p)}(\tilde{\mathbf{D}}_2^{(p)})^{-1}\tilde{\mathbf{D}}_3^{(p)})^{-1} & -(\tilde{\mathbf{D}}_1^{(p)})^{-1}\tilde{\mathbf{D}}_3^{(p)}(\tilde{\mathbf{D}}_2^{(p)} - \tilde{\mathbf{D}}_3^{(p)}(\tilde{\mathbf{D}}_1^{(p)})^{-1}\tilde{\mathbf{D}}_3^{(p)})^{-1}\\ -(\tilde{\mathbf{D}}_2^{(p)})^{-1}\tilde{\mathbf{D}}_3^{(p)}(\tilde{\mathbf{D}}_1^{(p)} - \tilde{\mathbf{D}}_3^{(p)}(\tilde{\mathbf{D}}_2^{(p)})^{-1}\tilde{\mathbf{D}}_3^{(p)})^{-1} & (\tilde{\mathbf{D}}_2^{(p)} - \tilde{\mathbf{D}}_3^{(p)}(\tilde{\mathbf{D}}_1^{(p)})^{-1}\tilde{\mathbf{D}}_3^{(p)})^{-1}\end{bmatrix} \tag{44}$$

of N-ADMM will reduce to $O(\log(\varepsilon^{-1})(8N^2+40N)+2M)$ at each iteration.

For comparison, the computational complexity of SDR-based methods are given as follows. The method of [17] is a standard SDR problem and its computational complexity is $O(\max\{M,N\}^4 N^{1/2}\log(\varepsilon_1^{-1}))$, where ε_1 is the solution accuracy [36]. The method of [16] is a iterated version of method [17], and its computational complexity is $O(\max\{M,N\}^4 N^{1/2}\log(\varepsilon_1^{-1})I_1)$, where I_1 is the predefined iteration number. The practical running times of all methods depend on the iteration numbers, and they will be compared with each other in Section V.

V. NUMERICAL EXAMPLES

In this section, simulation experiments are carried out to evaluate the effectiveness of the proposed approach.

The simulation parameters of airborne array radar are given in Table 3. We assume there exist 3 jammers and 5 true targets in the battle field, and each jammer generates 20 false targets with randomly assigned range-Doppler parameter. The locations of these targets in range-Doppler map are shown in Fig. 4. The other parameters of the jammers and true targets are given in Table 4. The target, deceptive jamming and clutter signals are generated according to (1), (5) and (4), respectively.

TABLE 3. Parameters of simulated airborne radar system.

Parameters	Symbols	Values
Operation wavelength	λ	0.2 m
PRF of sense waveform	f_{PRF}	5 kHz
Clutter-to-noise-ratio	CNR	40 dB
Velocity of the platform	v	125 m/s
Altitude of the platform	H	6000 m
Number of range bins	L	300
Element spacing	d	0.1 m
Number of antenna elements	N	32
Pulse number of sense waveform	K	64

TABLE 4. Parameters of true targets and deceptive jamming.

Signal type	DOA	SNR
True targets	0°	5 dB
Deceptive Jamming #1	−51°	40 dB
Deceptive Jamming #2	11°	35 dB
Deceptive Jamming #3	21°	35 dB

For the action stage, all notches are widened to 3° by adding angle grids around the estimated DOAs of jammers. The angle spacing of adjacent grids is 0.25°. The normalized notch depth is set as −55 dB. The maximum iteration number of N-ADMM is set as I =10000, and the outer termination condition of N-ADMM is set as $\Delta = 10^{-4}$. The absolute tolerance and relative tolerance of inner ADMM (of N-ADMM) are set as $\varepsilon^{\text{abs}} = 10^{-3}$ and $\varepsilon^{\text{rel}} = 10^{-2}$, respectively. The initialization of the N-ADMM is conducted as follows. Let $\tilde{\mathbf{w}}^{(0)} = \left[\Re\left\{\mathbf{a}^{\text{T}}(\vartheta_0)\right\}, \Im\left\{\mathbf{a}^{\text{T}}(\vartheta_0)\right\}\right]^{\text{T}}$, $\boldsymbol{\lambda}_0^{(0)} = 0$ and $\boldsymbol{\lambda}_m^{(0)} = 0$, then $\mathbf{y}_m^{(0)}$ and $\mathbf{y}_0^{(0)}$ can be determined by (32) and (39), respectively. The initialization of inner ADMM is performed as follows: $\mathbf{z}^{(0)} = 0$, $\boldsymbol{\beta}_1^{(0)} = 0$ and $\boldsymbol{\beta}_2^{(0)} = 0$.

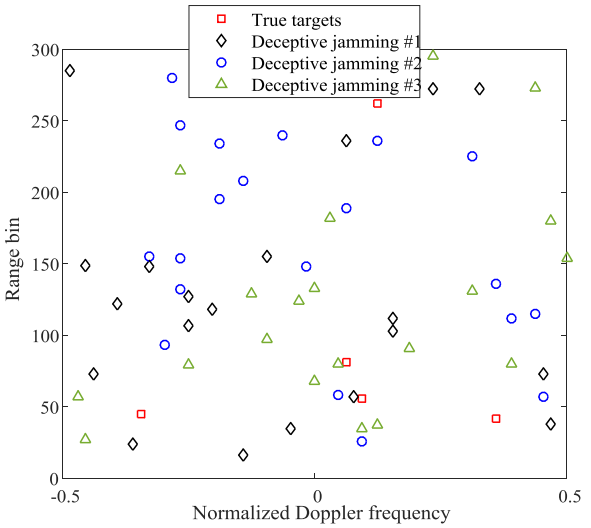

FIGURE 4. Distribution of the simulated targets in range-Doppler map.

A. RESULTS OF DECPTIVE JAMMING PERCEPTION

1) RESULT OF TARGET DETECTION

Fig. 5 depicts the range-Doppler map of PD processing, and the result of CFAR detection is also given in this plot. It can be seen that the Doppler bandwidth of clutter is about $f_{\text{PRF}}/2$, and one half of targets are located in clutter region. After CFAR detection, most of the targets (53 targets including true targets and false targets, marked with green cross) are detected out except those located close to or in mainlobe clutter region. Obviously, it is difficult to distinguish these

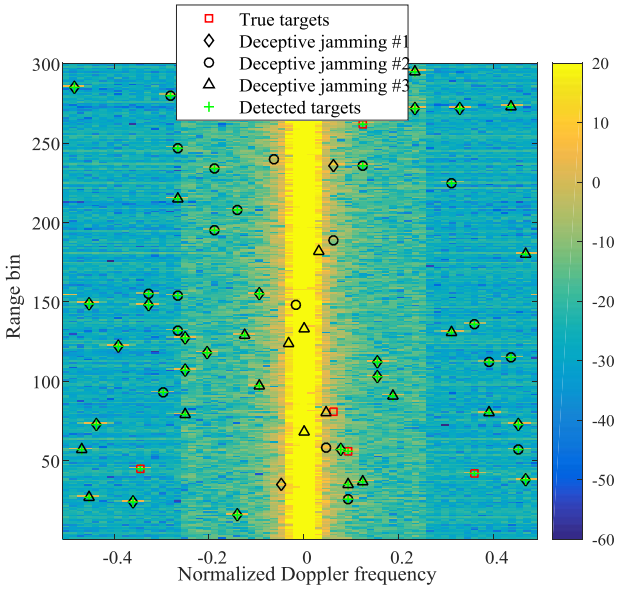

FIGURE 5. Results of PD processing and OS-CFAR detection.

detected targets only relying on the range or Doppler information. In the subsequence, the DOA of these detected targets will be estimated by ML algorithm (12), and then the deceptive jamming will be identified according to the algorithm proposed in Table 1.

2) RESULT OF DOA ESTIMATION

Fig. 6 shows the estimated DOAs of all detected targets. It is shown that the DOAs can be correctly estimated by the proposed ML algorithm, and the estimated DOAs are concentrated in four angle regions corresponding to the four signal sources. Subsequently, the deceptive jamming will be identified according to the angle clustering feature.

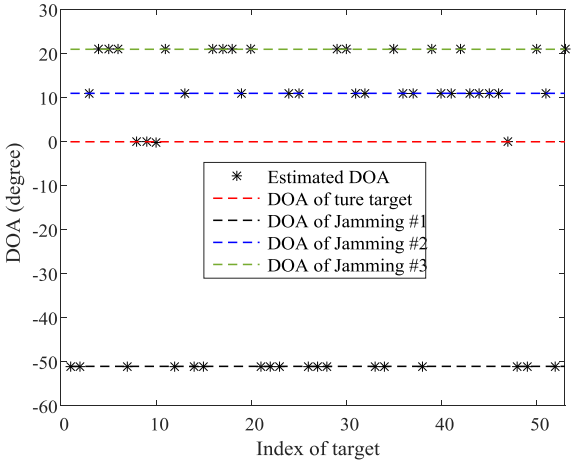

FIGURE 6. Estimated DOAs of the detected targets.

3) RESULT OF DECEPTIVE JAMMING IDENTIFICATION AND JAMMER LOCALIZATION

According to the algorithm presented in Table 1, the DOAs within mainbeam are firstly excluded from the DOA data set. The residual DOAs are given in Fig. 7. It can be seen that the DOAs corresponding to the true targets are removed, and the

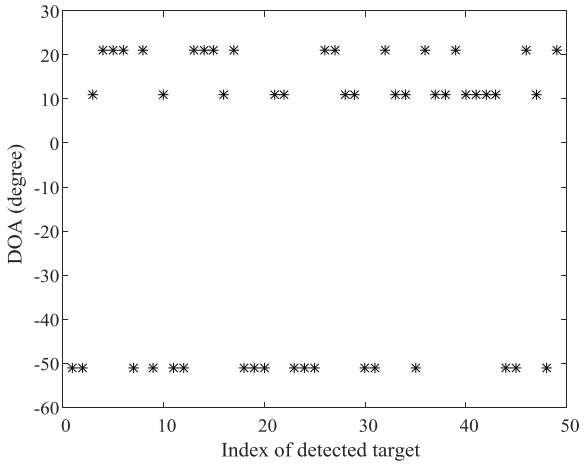

FIGURE 7. Residual DOAs after removing mainlobe targets.

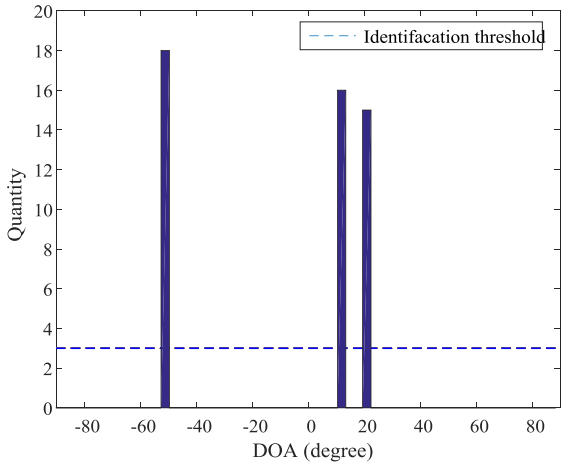

FIGURE 8. Histogram of the distribution of DOAs.

residual targets are false targets or false alarms. Fig. 8 shows the histogram of the distribution of the residual DOAs. It is shown that the DOAs are mainly located in three angle regions which corresponds to three jammers. With this observation, the deceptive jamming can be identified and classified by the proposed angle-clustering-feature-based classification algorithm. Running result shows there exist three different classes of deceptive jamming. Then, the directions of the jammers can be obtained by averaging the DOAs of every class. Finally, the DOAs of jammers are estimated as $-51.01°$, $10.98°$ and $21.02°$ respectively, which are quite approximate to the theoretic values. Subsequently, the estimated DOAs will be feed into the action stage for transmit pattern notching.

B. PERFORMANCE OF TRANSMIT PATTERN NOTCHING WITH N-ADMM

In this subsection, we will assess the performance of the proposed N-ADMM algorithm in terms of convergence, beampattern, magnitudes and running time. The results of SDP-based methods in [16] and [17] are also given for comparison. Both solution vectors of [16] and [17] are obtained by performing rank-1 decomposition of the resulting matrices.

1) BEAMPATTERN WITH NON-UNIMODULAR EXCITATIONS

Firstly, all algorithms are evaluated under the condition of non-unimodular excitations. The penalty parameters of outer ADMM and inner ADMM are set as $\rho = 0.2$ and $\rho_1 = 20$ respectively.

Fig. 9(a) shows the primal residual norms and stopping criterion limit of N-ADMM versus the iteration number. It can be seen that the termination condition of N-ADMM algorithm is met after 1523 iterations. Fig. 9(b) reveals the objective function values in (21) versus the iteration number. As illustrated in Fig. 9(b), the objective function is minimized at the 7th iteration. However, there exists a tiny gap between the steady value of the objective function and the optimal value. This may attribute to the fact that the solution needs

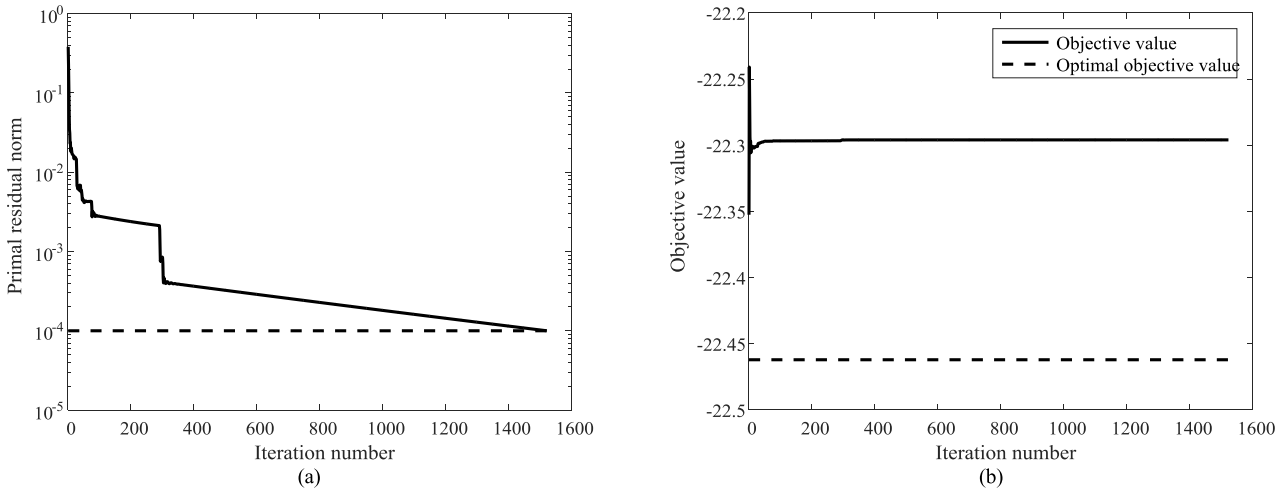

FIGURE 9. Residual norm and objective function value of N-ADMM under the non-unimodular condition. (a) Primal residual norm versus the iteration number. (b) Objective function value versus iteration number.

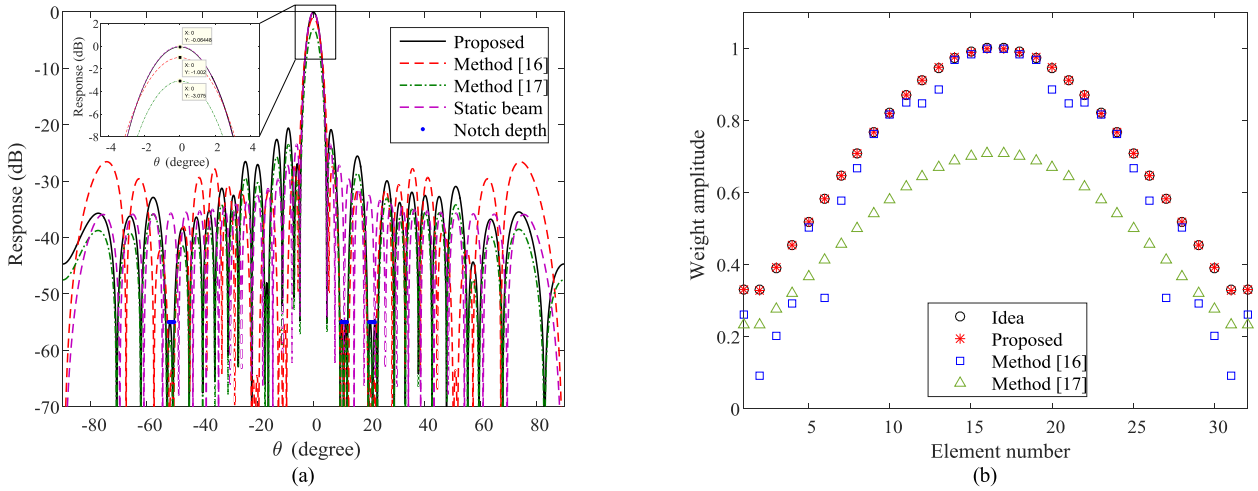

FIGURE 10. Beampatterns and amplitudes of weight vectors under the non-unimodular condition (a) Beampatterns of different methods. (b) Amplitudes of weight vectors of various methods.

to make a trade-off between the objective function value and amplitude constraints.

Fig. 10(a) gives the normalized beampatterns (to the theoretic array gain) of three different methods. The static sumbeam without notching is also illustrated for comparison. It is shown that all methods can place satisfied deep notches at the directions of jammers. However, as depicted in Fig. 10(a), the array gain loss of the proposed algorithm is only 0.064 dB, while the gain losses of the method [16] and method [17] are 1.002 dB and 3.082 dB respectively. The reason can be find in Fig. 10(b) which shows the amplitudes of each element of the solutions. It can be seen that the magnitudes of the proposed algorithm matches the given magnitudes very well, while the magnitudes of the method [16] and method [17] are lower than the given magnitudes. Therefore, the array gain losses of method [16] and method [17] are larger than that of the proposed method.

2) BEAMPATTERN WITH UNIMODULAR EXCITATIONS

Subsequently, all algorithms are assessed in the case of unimodular excitations. The penalty parameters of outer ADMM and inner ADMM are set as $\rho = 0.15$ and $\rho_1 = 20$ respectively.

Fig. 11(a) illustrates the primal residual norms and stopping criterion limit of N-ADMM versus the iteration number. It is shown that the termination condition of N-ADMM algorithm is met after 1185 iterations. Fig. 11(b) gives the objective function values in (21) versus the iteration number. It can be seen that the objective function is minimized at the 6th iteration. However, there exists a gap between the optimal value and steady value of the objective function. This phenomenon is similar to Fig. 9(b).

Fig. 12(a) gives the normalized beampatterns of three different methods. The static sumbeam without notching is also depicted for comparison. It is shown that all methods can

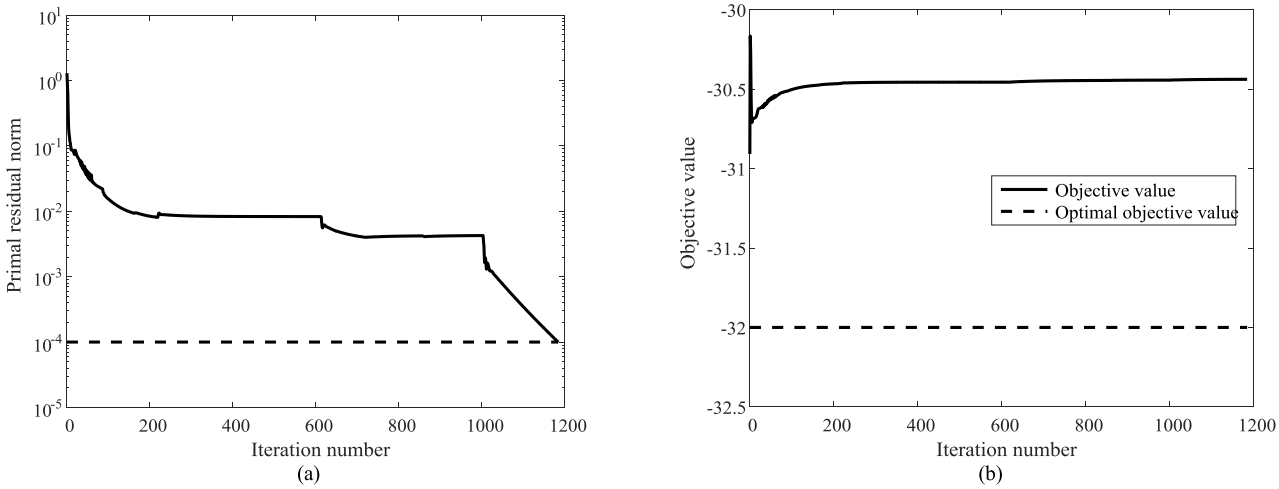

FIGURE 11. Residual norm and objective function value of N-ADMM under the unimodular condition. (a) Primal residual norm versus the iteration number. (b) Objective function value versus iteration number.

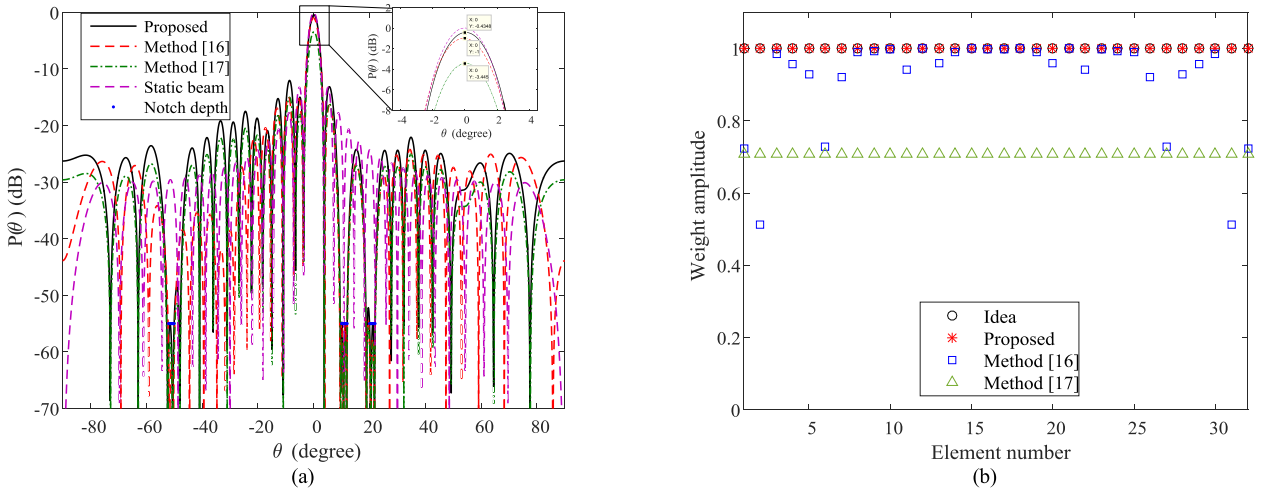

FIGURE 12. Beampatterns and amplitudes of weight vectors under the unimodular condition (a) Beampatterns of different methods. (b) Amplitudes of weight vectors of various methods.

introduce required deep notches at the directions of jammers. However, as revealed in Fig. 12(a), the gain loss of the proposed algorithm is only 0.435 dB, while the gain losses of the method [16] and method [17] are 1.0 dB and 3.445 dB respectively. Fig. 12(b) exhibits the magnitudes of each element of the solutions. It can be seen that the magnitudes of the proposed algorithm matches the given magnitudes very well, while the magnitudes of the method [16] and method [17] are much lower than the given magnitudes. Therefore, the array gain loss of the proposed method is smaller than those of method [16] and method [17].

3) RUNNING TIME

In order to evaluate the efficiency of the proposed N-ADMM algorithm, the running time is tested under the scenarios of unimodular constraint and non-unimodular constraint. All the numerical examples are analyzed using matlab 2015b version, perfoming on a standard PC (with 2.5 GHz of double-core CPU and 4 GB of RAM). Table 5 gives the running time of the proposed algorithm under different conditions. The results of method [16] and method [17] are also given for comparison, where the optimization problems in [16] and [17] are both solved by CVX toolbox [22], and the iteration number of method [16] is set as 5. It is shown that the proposed algorithm has the shortest running time, meanwhile it possesses the best performance (in terms of gain loss and magnitudes).

TABLE 5. Running time with different conditions.

Algorithm	N-ADMM	Method [16]	Method [17]
Running time (s) with unimodular constraint	1.559	15.038	2.476
Running time (s) with non-unimodular constraint	2.123	16.384	2.650

C. INFLUENCE ON STAP

In this part, we will examine the impact of the proposed anti-jamming scheme on STAP. In order to enhance the robustness

of STAP in dense targets environment, the NHD is used to exclude the non-homogeneous samples (i.e., the range bins involving true target or false target) before covariance matrix estimating [23]. Fig. 13 illustrates the STAP results of the 41th Doppler bin (the corresponding normalized Doppler frequency is 0.125) with and without active anti-jamming measures. Only the outputs of the 225-th to the 275-th range bins are given in this figure. It can be seen that, in the case of absence of active anti-jamming measure, although STAP can suppress the clutter, it is failed to reject the deceptive jamming. In contrast, if we take active anti-jamming measure, the received signal will not include deceptive jamming (we assume the radar signal cannot be intercepted by the jammers). Therefore, as illustrated in Fig. 13, the output of STAP does not contain false target. This will be a great benefit to the subsequent data processing (such as target tracking).

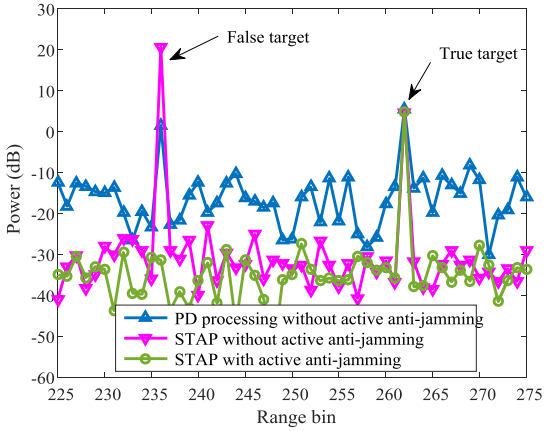

FIGURE 13. Filtering outputs of STAP in different scenarios.

VI. CONCLUSION

In this paper, the problem of anti-deception jamming in an airborne array radar is considered. A cognitive transmit pattern notching scheme is proposed to deal with the above problem. The proposed approach mainly consists of two parts, i.e., deceptive jamming perception and transmit pattern notching.

In the perception stage, the sensing waveform parameter is rationally designed to enhance the performance of target detection and DOA estimation. Then, the deceptive jamming is identified according to the angle-clustering feature. Finally, the directions of jammers are determined by averaging the classified DOAs.

In the action stage, the transmit pattern is designed with notches at the jammers' directions. The encountered problem is virtually a nonconvex QCLP problem. A N-ADMM algorithm with closed-form solutions at every iteration is proposed to cope with this problem. Simulation results shows that the proposed approach is valid in different conditions. The proposed N-ADMM can also be applied to other analogous QCLP problems. Although the proposed phase-only pattern synthesis algorithm has lower computational complexity, less gain loss and more accurate magnitudes, its sidelobe level is slightly higher than those of the existing methods.

In this work, we mainly consider the problem of anti-sidelobe deceptive jamming. Future research area may focus on anti-mainlobe deceptive jamming using other resources of the radar system.

APPENDIX
UPDATE $\tilde{\mathbf{w}}$ USING ADMM

To solve the optimization problem of (24), we first rewrite the amplitude constraints as

$$\tilde{\mathbf{w}}^{\mathrm{T}}\mathbf{E}_n\tilde{\mathbf{w}} = c_n^2, \quad n = 1, \cdots, N, \tag{A.1}$$

where $\mathbf{E}_n \in \mathbb{R}^{2N\times 2N}$ is a sparse matrix with all elements being zeros except the (n, n)-th and the $(n+N, n+N)$-th elements equal to one.

By introducing an auxiliary primal variable $\mathbf{z} \in \mathbb{R}^{2N\times 1}$, problem (24) can be equivalently expressed as

$$\begin{aligned} &\min_{\tilde{\mathbf{w}}} \tilde{\mathbf{w}}^{\mathrm{T}}\mathbf{R}_1\mathbf{z} + \tilde{\mathbf{w}}^{\mathrm{T}}\mathbf{d}_1^{(i)} \\ &\text{s.t. } \mathbf{z} = \tilde{\mathbf{w}} \\ &\quad \tilde{\mathbf{w}}^{\mathrm{T}}\mathbf{E}_n\mathbf{z} = c_n^2, \quad n = 1, \cdots, N. \end{aligned} \tag{A.2}$$

The last N equality constraints of (A.2) can be expressed in a compact form:

$$\mathbf{g}(\mathbf{z}, \tilde{\mathbf{w}}) = \mathbf{G}\left(\tilde{\mathbf{w}}\right)\mathbf{z} = \mathbf{B}\left(\mathbf{z}\right)\tilde{\mathbf{w}} = \mathbf{c}_0, \tag{A.3}$$

where $\mathbf{g}(\mathbf{z}, \tilde{\mathbf{w}}) = \mathbf{c}_0 \in \mathbb{R}^{N\times 1}$, and $\mathbf{G}\left(\tilde{\mathbf{w}}\right) \in \mathbb{R}^{N\times 2N}$, $\mathbf{B}\left(\mathbf{z}\right) \in \mathbb{R}^{N\times 2N}$ and $\mathbf{c}_0 \in \mathbb{R}^{N\times 1}$, which are given by

$$\mathbf{G}\left(\tilde{\mathbf{w}}\right) = \left[\mathbf{E}_1\tilde{\mathbf{w}}, \cdots, \mathbf{E}_N\tilde{\mathbf{w}}\right]^{\mathrm{T}}, \tag{A.4}$$

$$\mathbf{B}\left(\mathbf{z}\right) = \left[\mathbf{z}^{\mathrm{T}}\mathbf{E}_1; \cdots; \mathbf{z}^{\mathrm{T}}\mathbf{E}_N\right], \tag{A.5}$$

$$\mathbf{c}_0 = \left[c_1^2, \cdots, c_N^2\right]^{\mathrm{T}}. \tag{A.6}$$

Note that the objective function and constraints in (A.2) are now jointly affine in $\mathbf{z}$ and $\tilde{\mathbf{w}}$. Therefore, the ADMM algorithm is very suitable for finding the solution of problem (A.2).

The augmented Lagrangian of (A.2) can be constructed as

$$\begin{aligned} &\ell_{1,\rho_1}\left(\tilde{\mathbf{w}}, \mathbf{z}, \boldsymbol{\beta}_1, \boldsymbol{\beta}_2\right) \\ &= \tilde{\mathbf{w}}^{\mathrm{T}}\mathbf{R}_1\mathbf{z} + \tilde{\mathbf{w}}^{\mathrm{T}}\mathbf{d}_1^{(i)} + \left(\boldsymbol{\beta}_1^{\mathrm{T}}\left(\mathbf{z} - \tilde{\mathbf{w}}\right) + \frac{\rho_1}{2}\left\|\mathbf{z} - \tilde{\mathbf{w}}\right\|^2\right) \\ &\quad + \left(\boldsymbol{\beta}_2^{\mathrm{T}}\left(\mathbf{g}(\mathbf{z}, \tilde{\mathbf{w}}) - \mathbf{c}_0\right) + \frac{\rho_1}{2}\left\|\mathbf{g}(\mathbf{z}, \tilde{\mathbf{w}}) - \mathbf{c}_0\right\|^2\right), \end{aligned} \tag{A.7}$$

where $\boldsymbol{\beta}_1 \in \mathbb{R}^{2N\times 1}$ and $\boldsymbol{\beta}_2 \in \mathbb{R}^{N\times 1}$ are the Lagrange multiplier vectors, while $\rho_1 > 0$ is a user-defined parameter representing the primal step size. Then all unknowns in (A.7) as well as $\boldsymbol{\beta}_1$ and $\boldsymbol{\beta}_2$ can be determined using the iterative manner of the ADMM from $\ell_{1,\rho_1}\left(\tilde{\mathbf{w}}, \mathbf{z}, \boldsymbol{\beta}_1, \boldsymbol{\beta}_2\right)$:

Step 1: Update $\tilde{\mathbf{w}}$ with given $\left\{\mathbf{z}^{(p)}, \boldsymbol{\beta}_1^{(p)}, \boldsymbol{\beta}_2^{(p)}\right\}$ (which are obtained from the p-th iteration) by solving

$$\min_{\tilde{\mathbf{w}}} \ \ell_{1,\rho_1}\left(\tilde{\mathbf{w}}, \mathbf{z}^{(p)}, \boldsymbol{\beta}_1^{(p)}, \boldsymbol{\beta}_2^{(p)}\right). \tag{A.8}$$

The gradient of $\ell_{1,\rho_1}\left(\tilde{\mathbf{w}}, \mathbf{z}^{(p)}, \boldsymbol{\beta}_1^{(p)}, \boldsymbol{\beta}_2^{(p)}\right)$ with respect to $\tilde{\mathbf{w}}$ is

$$\nabla_{\tilde{\mathbf{w}}}\ell_{1,\rho_1}\left(\tilde{\mathbf{w}}, \mathbf{z}^{(p)}, \boldsymbol{\beta}_1^{(p)}, \boldsymbol{\beta}_2^{(p)}\right) = \mathbf{R}_2^{(p)}\tilde{\mathbf{w}} + \mathbf{d}_2^{(p)}, \tag{A.9}$$

where

$$\mathbf{R}_2^{(p)} = \rho_1 \left(\mathbf{I}_{2N} + \mathbf{B}^{\mathrm{T}} \left(\mathbf{z}^{(p)} \right) \mathbf{B} \left(\mathbf{z}^{(p)} \right) \right) \tag{A.10}$$

and

$$\mathbf{d}_2^{(p)} = \left(\mathbf{R}_1 - \rho_1 \mathbf{I}_{2N} \right) \mathbf{z}^{(p)} + \mathbf{B}^{\mathrm{T}} \left(\mathbf{z}^{(p)} \right) \left(\boldsymbol{\beta}_2^{(p)} - \rho_1 \mathbf{c}_0 \right) + \mathbf{d}_1^{(i)} - \boldsymbol{\beta}_1^{(p)}. \tag{A.11}$$

To find the global minimization of (A.8), we need to solve the equation

$$\nabla_{\tilde{\mathbf{w}}} \ell_{1,\rho_1} \left(\tilde{\mathbf{w}}, \mathbf{z}^{(p)}, \boldsymbol{\beta}_1^{(p)}, \boldsymbol{\beta}_2^{(p)} \right) = \mathbf{R}_2^{(p)} \tilde{\mathbf{w}} + \mathbf{d}_2^{(p)} = 0. \tag{A.12}$$

Therefore, the close-form solution of (A.12), i.e., the optimal solution of (A.8) can be obtained as

$$\tilde{\mathbf{w}}^{(p+1)} = - \left(\mathbf{R}_2^{(p)} \right)^{-1} \mathbf{d}_2^{(p)}. \tag{A.13}$$

Step 2: Update $\mathbf{z}$ with given $\left\{ \tilde{\mathbf{w}}^{(p+1)}, \boldsymbol{\beta}_1^{(p)}, \boldsymbol{\beta}_2^{(p)} \right\}$ by solving

$$\min_{\mathbf{z}} \quad \ell_{1,\rho_1} \left(\tilde{\mathbf{w}}^{(p+1)}, \mathbf{z}, \boldsymbol{\beta}_1^{(p)}, \boldsymbol{\beta}_2^{(p)} \right). \tag{A.14}$$

Similarly to **Step** 1, we first calculate the gradient of $\ell_{1,\rho_1} \left(\tilde{\mathbf{w}}^{(p+1)}, \mathbf{z}, \boldsymbol{\beta}_1^{(p)}, \boldsymbol{\beta}_2^{(p)} \right)$ with respect to $\mathbf{z}$, i.e.,

$$\nabla_{\mathbf{z}} \ell_{1,\rho_1} \left(\tilde{\mathbf{w}}^{(p+1)}, \mathbf{z}, \boldsymbol{\beta}_1^{(p)}, \boldsymbol{\beta}_2^{(p)} \right) = \mathbf{R}_3^{(p)} \tilde{\mathbf{w}} + \mathbf{d}_3^{(p)}, \tag{A.15}$$

where

$$\mathbf{R}_3^{(p)} = \rho_1 \left(\mathbf{I}_{2N} + \mathbf{G}^{\mathrm{T}} \left(\tilde{\mathbf{w}}^{(p+1)} \right) \mathbf{G} \left(\tilde{\mathbf{w}}^{(p+1)} \right) \right) \tag{A.16}$$

and

$$\mathbf{d}_3^{(p)} = \left(\mathbf{R}_1 - \rho_1 \mathbf{I}_{2N} \right) \tilde{\mathbf{w}}^{(p+1)} + \mathbf{G}^{\mathrm{T}} \left(\tilde{\mathbf{w}}^{(p+1)} \right) \left(\boldsymbol{\beta}_2^{(p)} - \rho_1 \mathbf{c}_0 \right) + \boldsymbol{\beta}_1^{(p)}. \tag{A.17}$$

To find the global minimization of (A.14), we need to solve the equation

$$\nabla_{\mathbf{z}} \ell_{1,\rho_1} \left(\tilde{\mathbf{w}}^{(p+1)}, \mathbf{z}, \boldsymbol{\beta}_1^{(p)}, \boldsymbol{\beta}_2^{(p)} \right) = \mathbf{R}_3^{(p)} \tilde{\mathbf{w}} + \mathbf{d}_3^{(p)} = 0. \tag{A.18}$$

Therefore, the optimal solution of (A.14) can be obtained as

$$\mathbf{z}^{(p+1)} = - \left(\mathbf{R}_3^{(p)} \right)^{-1} \mathbf{d}_3^{(p)}. \tag{A.19}$$

Step 3: Update $\boldsymbol{\beta}_1$ and $\boldsymbol{\beta}_2$ as

$$\boldsymbol{\beta}_1^{(p+1)} = \boldsymbol{\beta}_1^{(p)} + \rho_1 \left(\mathbf{z}^{(p+1)} - \tilde{\mathbf{w}}^{(p+1)} \right), \tag{A.20}$$

$$\boldsymbol{\beta}_2^{(p+1)} = \boldsymbol{\beta}_2^{(p)} + \rho_1 \left(\mathbf{g}(\mathbf{z}^{(p+1)}, \tilde{\mathbf{w}}^{(p+1)}) - \mathbf{c}_0 \right). \tag{A.21}$$

By iterating **Steps** 1 to 3 until satisfying termination criteria, we can obtain the updated $\tilde{\mathbf{w}}^{(i+1)}$.

The termination criterion is set to be the same as [35]. More specifically, we first define

$$\mathbf{d}_{\mathrm{r1}}^{(p+1)} = \mathbf{z}^{(p+1)} - \tilde{\mathbf{w}}^{(p+1)}, \tag{A.22}$$

$$\mathbf{d}_{\mathrm{r2}}^{(p+1)} = \mathbf{g}(\mathbf{z}^{(p+1)}, \tilde{\mathbf{w}}^{(p+1)}) - \mathbf{c}_0 \tag{A.23}$$

as the primal residuals at $p+1$ iteration and

$$\mathbf{d}_{\mathrm{s}}^{(p+1)} = \rho_1 (\tilde{\mathbf{w}}^{(p+1)} - \tilde{\mathbf{w}}^{(p)}) \tag{A.24}$$

as dual residual at $p+1$ iteration, respectively. [35] suggests that a group of reasonable termination criteria are

$$\left\| \mathbf{d}_{\mathrm{r1}}^{(p)} \right\| \leq \varepsilon_1^{\mathrm{pri}}, \quad \left\| \mathbf{d}_{\mathrm{r2}}^{(p)} \right\| \leq \varepsilon_2^{\mathrm{pri}} \text{ and } \left\| \mathbf{d}_{\mathrm{s}}^{(p)} \right\| \leq \varepsilon^{\mathrm{dual}}, \tag{A.25}$$

where $\varepsilon_1^{\mathrm{pri}}$, $\varepsilon_2^{\mathrm{pri}}$ and $\varepsilon^{\mathrm{dual}}$ are the tolerances for primal residuals and dual residual, which are defined as

$$\varepsilon_1^{\mathrm{pri}} = \sqrt{2N} \varepsilon^{\mathrm{abs}} + \varepsilon^{\mathrm{rel}} \max \left\{ \left\| \mathbf{z}^{(p)} \right\|, \left\| \tilde{\mathbf{w}}^{(p)} \right\| \right\}, \tag{A.26}$$

$$\varepsilon_2^{\mathrm{pri}} = \sqrt{N} \varepsilon^{\mathrm{abs}} + \varepsilon^{\mathrm{rel}} \max \left\{ \left\| \mathbf{g}(\mathbf{z}^{(p)}, \tilde{\mathbf{w}}^{(p)}) \right\|, \| \mathbf{c}_0 \| \right\}, \tag{A.27}$$

$$\varepsilon^{\mathrm{dual}} = \sqrt{2N} \varepsilon^{\mathrm{abs}} + \varepsilon^{\mathrm{rel}} \left\| \boldsymbol{\beta}_1^{(p)} \right\|, \tag{A.28}$$

where $\varepsilon^{\mathrm{abs}}$ is a absolute tolerance and $\varepsilon^{\mathrm{rel}}$ is a relative tolerance.

REFERENCES

[1] R. Klemm, *Applications of Space-Time Adaptive Processing*. London, U.K.: IET, 2004.

[2] W. L. Melvin, "A STAP overview," *IEEE Aerosp. Electron. Syst. Mag.*, vol. 19, no. 1, pp. 19–35, Jan. 2004.

[3] D. Cerutti-Maori and I. Sikaneta, "A generalization of DPCA processing for multichannel SAR/GMTI radars," *IEEE Trans. Geosci. Remote Sens.*, vol. 5, no. 1, pp. 560–572, Jan. 2013.

[4] C. Wen, J. Peng, Y. Zhou, and J. Wu, "Enhanced three-dimensional joint domain localized STAP for airborne FDA-MIMO radar under dense false-target jamming scenario," *IEEE Sensors J.*, vol. 18, no. 10, pp. 4154–4166, May 2018.

[5] S. D. Berger, "Digital radio frequency memory linear range gate stealer spectrum," *IEEE Trans. Aerosp. Electron. Syst.*, vol. 39, no. 2, pp. 725–735, Apr. 2003.

[6] A. Farina, "Electronic Counter-countermeasures," in *Radar Handbook*, M. Skolnik, 3rd ed. New York, NY, USA: McGraw-Hill, 2008.

[7] J. Ward, "Space-time adaptive processing for airborne radar," Lincoln Labs, Lexington, MA, USA, Tech. Rep. 1015, Dec. 1994, pp. 20–24.

[8] H. Dai, X. Wang, Y. Li, Y. Liu, and S. Xiao, "Main-lobe jamming suppression method of using spatial polarization characteristics of antennas," *IEEE Trans. Aerosp. Electron. Syst.*, vol. 48, no. 3, pp. 2167–2179, Jul. 2012.

[9] B. Rao, S. Xiao, X. Wang, and T. Wang, "Maximum likelihood approach to the estimation and discrimination of exoatmospheric active phantom tracks using motion features," *IEEE Trans. Aerosp. Electron. Syst.*, vol. 48, no. 1, pp. 794–819, Jan. 2012.

[10] M. Nouri, M. Mivehchy, and M. F. Sabahi, "Target recognition based on phase noise of received signal," *Electron. Lett.*, vol. 53, no. 12, pp. 808–810, Jun. 2017.

[11] D. L. Adamy, *Electronic Warfare Against a New Generation of Threats*. Norwood, MA, USA: Artech House, 2015.

[12] J. Akhtar, "Orthogonal block coded ECCM schemes against repeat radar jammers," *IEEE Trans. Aerosp. Electron. Syst.*, vol. 45, no. 3, pp. 1218–1226, Jul. 2009.

[13] J. Zhang, D. Zhu, and G. Zhang, "New antivelocity deception jamming technique using pulses with adaptive initial phases," *IEEE Trans. Aerosp. Electron. Syst.*, vol. 49, no. 2, pp. 1290–1300, Apr. 2013.

[14] P. Cao, J. S. Thompson, and H. Haas, "Constant modulus shaped beam synthesis via convex relaxation," *IEEE Antennas Wireless Propag. Lett.*, vol. 16, pp. 617–620, 2017.

[15] J. Liang, X. Fan, Wen Fan, D. Zhou, and J. Li, "Phase-only pattern synthesis for linear antenna arrays," *IEEE Antennas Wireless Propag. Lett.*, vol. 16, pp. 3232–3235, 2017.

[16] B. Fuchs, "Application of convex relaxation to array synthesis problems," *IEEE Trans. Antennas Propag.*, vol. 62, no. 2, pp. 634–640, Feb. 2014.

[17] P. J. Kajenski, "Phase only antenna pattern notching via a semidefinite programming relaxation," *IEEE Trans. Antennas Propag.*, vol. 60, no. 5, pp. 2562–2565, May 2012.

[18] S. Haykin, "Cognitive radar: A way of the future," *IEEE Signal Process. Mag.*, vol. 23, no. 1, pp. 30–40, Jan. 2006.
[19] J. R. Guerci, *Cognitive Radar: The Knowledge Aided Fully Adaptive Approach*. Norwood, MA, USA: Artech House, 2010.
[20] M. S. Greco, F. Gini, and P. Stinco, "Cognitive radars: Some applications," in *Proc. IEEE Global Conf. Signal Inf. Process.*, Dec. 2016, pp. 1077–1082.
[21] J. Liang, H. C. So, J. Li, A. Farina, and D. Zhou, "On optimizations with magnitude constraints on frequency or angular responses," *Signal Process.*, vol. 145, pp. 214–224, Apr. 2018.
[22] M. Grant and S. Boyd. (Feb. 2016). *CVX: MATLAB Software for Disciplined Convex Programming, Version 2.1*. [Online]. Available: http://cvxr.com/cvx.
[23] M. Rangaswamy, J. H. Michels, and B. Himed, "Statistical analysis of the non-homogeneity detector for STAP applications," *Digit. Signal Process.*, vol. 14, no. 3, pp. 253–267, May 2004.
[24] H. Rohling, "Radar CFAR thresholding in clutter and multiple target situations," *IEEE Trans. Aerosp. Electron. Syst.*, vol. 19, no. 4, pp. 608–621, Jul. 1983.
[25] S. A. Villar, M. De Paula, F. J. Solari, and G. G. Acosta, "A framework for acoustic segmentation using order statistic-constant false alarm rate in two dimensions from sidescan sonar data," *IEEE J. Ocean. Eng.*, vol. 43, no. 3, pp. 735–748, Jul. 2018.
[26] E. D. Di Claudio, R. Parisi, and G. Jacovitti, "Space time MUSIC: Consistent signal subspace estimation for wideband sensor arrays," *IEEE Trans. Signal Process.*, vol. 66, no. 10, pp. 2685–2699, May 2018.
[27] C. Qian, "A simple modification of ESPRIT," *IEEE Signal Process. Lett.*, vol. 25, no. 8, pp. 1256–1260, Aug. 2018.
[28] J. Xu, W.-Q. Wang, and R. Gui, "Computational efficient DOA, DOD, and Doppler estimation algorithm for MIMO radar," *IEEE Signal Process. Lett.*, vol. 26, no. 1, pp. 44–48, Jan. 2019.
[29] J. H. G. Ender, "On compressive sensing applied to radar," *Signal Process.*, vol. 90, no. 5, pp. 1402–1414, May 2010.
[30] Z. Yang, L. Xie, and C. Zhang, "Off-grid direction of arrival estimation using sparse Bayesian inference," *IEEE Trans. Signal Process.*, vol. 61, no. 1, pp. 38–43, Jan. 2013.
[31] V. Nagesha and S. Kay, "Maximum likelihood estimation for array processing in colored noise," *IEEE Trans. Signal Process.*, vol. 44, no. 2, pp. 169–180, Feb. 1996.
[32] M. Li and Y. Lu, "Maximum likelihood DOA estimation in unknown colored noise fields," *IEEE Trans. Aerosp. Electron. Syst.*, vol. 44, no. 3, pp. 1079–1090, Jul. 2008.
[33] S. Boyd and L. Vandenberghe, *Convex Optimization*. Cambridge, U.K.: Cambridge Univ. Press, 2004.
[34] X. D. Zhang, *Matrix Analysis and Applications*. Cambridge, U.K.: Cambridge Univ. Press, 2017.
[35] S. Boyd, N. Parikh, E. Chu, B. Peleato, and J. Eckstein, "Distributed optimization and statistical learning via the alternating direction method of multipliers," *Found, Trends Mach. Learn.*, vol. 3, no. 1, pp. 1–122, 2011.
[36] Z.-Q. Luo, W.-K. Ma, A. M.-C. So, Y. Ye, and S. Zhang, "Semidefinite relaxation of quadratic optimization problems," *IEEE Signal Process. Mag.*, vol. 27, no. 3, pp. 20–34, May 2010.

CAI WEN (M'19) received the B.E. and Ph.D. degrees in signal and information processing from Xidian University, Xi'an, China, in 2009 and 2014, respectively.

He was a Research Scientist with the Xi'an Electronic Engineering Research Institute, from January 2015 to October 2016. He is currently an Assistant Professor with the School of Information Science and Technology, Northwest University. His research interests include space-time adaptive processing, array signal processing, mathematical optimization, and machine learning with applications in radar signal processing.

YAN HUANG (M'19) was born in Shandong, China, in 1991. He received the B.S. degree in electrical engineering, and the Ph.D. degree in signal and information processing from Xidian University, Xi'an, China, in 2013 and 2018, respectively.

He was a Visiting Ph.D. Student with the Electrical and Computer Engineering Department, University of Florida, from September 2016 to July 2017, and with the Electrical and Systems Engineering Department, Washington University in St. Louis, from July 2017 to August 2018. He is currently an Assistant Professor with the State Key Laboratory of Millimeter Waves, Southeast University. His research interests include machine learning, synthetic aperture radar, image processing, and ground moving target indication.

JIANXIN WU received the B.E. and Ph.D. degrees in signal and information processing from the Xidian University, Xi'an, China, in 2003 and 2009, respectively.

He is currently an Associate Professor with the School of Electronics and Communication Engineering, Sun Yat-sen University. His research interests include space-time adaptive processing and general radar signal processing.

JINYE PENG received the M.S. degree in computer science from Northwestern University, Xi'an, China, in 1996, and the Ph.D. degree from Northwestern Polytechnical University, Xi'an, in 2002.

He joined Northwest University as a Professor, in 2006. His research interests include statistical signal processing, image processing, and machine learning.

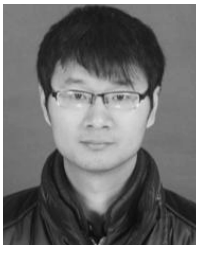

YAN ZHOU received the B.S. and Ph.D. degrees both from Xidian University, Xi'an, China, in 2010 and 2015, respectively.

He is currently a Lecturer with the School of Information Science and Technology, Northwest University. His research interests include space-time adaptive processing and MIMO radar signal processing.

JIE LIU received the M.Sc. degree in electrical circuit and system from Xidian University, Xi'an, China, in 2012.

She is currently an Engineer with Xi'an Institute of Space Radio Technology. Her research interests include space wireless communications, high-speed signal sampling, and analog/mixed-signal circuits design.